Experimental Study of Main Gas Ingestion

in a Subscale 1.5-stage Axial Flow Air Turbine

by

Mukilan Sebastiraj Michael

A Thesis Presented in Partial Fulfillment
of the Requirements for the Degree
Master of Science

Approved November 2015 by the
Graduate Supervisory Committee:

Ramendra P. Roy, Co-Chair
Marc Mignolet, Co-Chair
Patrick Phelan

ARIZONA STATE UNIVERSITY

December 2015

ABSTRACT

Gas turbine efficiency has improved over the years due to increases in compressor pressure ratio and turbine entry temperature (TET) of main combustion gas, made viable through advancements in material science and cooling techniques. Ingestion of main combustion gas into the turbine rotor-stator disk cavities can cause major damage to the gas turbine. To counter this ingestion, rim seals are installed at the periphery of turbine disks, and purge air extracted from the compressor discharge is supplied to the disk cavities. Optimum usage of purge air is essential as purge air extraction imparts a penalty on turbine efficiency and specific fuel consumption.

In the present work, experiments were conducted in a newly constructed 1.5-stage axial flow air turbine featuring vanes and blades to study main gas ingestion. The disk cavity upstream of the rotor, the 'front cavity', features a double seal with radial clearance and axial overlap at its rim. The disk cavity downstream of the rotor, the 'aft cavity', features a double seal at its rim but with axial gap. Both cavities contain a labyrinth seal radially inboard; this divides each disk cavity into an 'inner cavity' and a 'rim cavity'.

Time-averaged static pressure at various locations in the main gas path and disk cavities, and tracer gas (CO_2) concentration at different locations in the cavities were measured. Three sets of experiments were carried out; each set is defined by the main air flow rate and rotor speed. Each of the three sets comprises of four different purge air flow rates, low to high.

The mass flow rate of ingested main gas into the front and aft rim cavities is reported at the different purge air flow rates, for the three experiment sets. For the present stage configuration, it appears that some ingestion persisted into both the front and aft rim

cavities even at high purge air flow rates. On the other hand, the front and aft inner cavity were completely sealed at all purge flows.

DEDICATION

To

Appa, Amma, Manoj and Mithran

ACKNOWLEDGMENTS

First and foremost I would like to thank Prof. Ramendra P. Roy for giving me the opportunity to work on this project and for his guidance throughout the course of this project. I thank Prof. Marc Mignolet and Prof. Patrick Phelan for having agreed to be on my thesis committee.

I express my sincere gratitude to Jagdish Harihara Balasubramanian for providing constant support and guidance selflessly throughout the project. His contribution to this work is greatly acknowledged. Thanks are due to Prashanth Singh for his contribution during the initial phase of this project.

I would like to extend my gratitude to the personnel of Engineering Technical Services (Dennis Golabiewski, Martin Johnson, David Mushier, Ben Schwatken and Brian Ipema) who were always ready to help. Their contribution to the success of this project is greatly appreciated.

I owe my heartfelt gratitude to my parents and brothers for always being a great source of moral support in my endeavors. My special thanks are due to my friends and Prof. Walter Higgins and his family, for their support and guidance in the due course of this project.

The grant from Solar Turbines Inc. for this research work is gratefully acknowledged.

TABLE OF CONTENTS

Page

LIST OF TABLES

LIST OF FIGURES

NOMENCLATURE

C	Time-averaged CO_2 Mass Concentration (%)
C_d	Coefficient of Discharge
c_w	Dimensionless Mass Flow Rate of Purge Air = $\frac{\dot{m}_{purge}}{\mu R_h}$
$c_{w,egress}$	Dimensionless Mass Flow Rate of Egress Air = $\frac{\dot{m}_{egress}}{\mu R_h}$
$c_{w,ing}$	Dimensionless Mass Flow Rate of Ingested Air = $\frac{\dot{m}_{ing}}{\mu R_h}$
$c_{w,min}$	Dimensionless Minimum Purge Air Flow Required to Prevent Ingestion
C_{vax}	Vane Axial Chord Length (m)
G	Dimensionless Disk Cavity Axial Gap = $\frac{s}{R_h}$
G_c	Dimensionless Rim Seal Gap = $\frac{s_c}{R_h}$
G_{cax}	Dimensionless Rim Seal Axial Gap = $\frac{s_{cax}}{R_h}$
G_{cr}	Dimensionless Rim Seal Radial Clearance = $\frac{s_{cr}}{R_h}$
$\dot{m}$	Mass Flow Rate of Air (kg/s)
P	Pressure (Pa)
Q	Volumetric Air Flow Rate (m^3/s)
R_h	Rotor Blade Hub Radius (mm)
$R_{N2,hub}$	N2 Vane Hub Radius (mm)
$R_{N3,hub}$	N3 Vane Hub Radius (mm)

$R_{N2,N3\ tip}$	N2 Vane and N3 Vane Tip Radius (mm)
Re_{vax}	Main Air Flow Reynolds Number Based on $C_{vax,} = \rho V_{a2} C_{vax}/\mu$
Re_{R_h}	Main Air Flow Reynolds number Based on $R_h, = \rho V_{a2} R_h/\mu$
Re_{ϕ}	Rotor Disk Rotational Reynolds Number, $= \rho \Omega R_h^2/\mu$
$\underline{r}$	Radial Position Vector
r	Radial Coordinate with Origin at Rotor/Stator Axis
s	Disk Cavity Axial Gap (mm)
s_c	Rim Seal Gap (mm)
s_{cax}	Rim Seal Axial Gap (mm)
s_{cr}	Rim Seal Radial Clearance (mm)
U	Blade Hub Speed (m/s)
$V_{rim\ seal}$	Velocity of Air tThrough Rim Seal Gap (m/s)
V_{a2}	Mixed-mean Axial Velocity of Main Air in Annulus Immediately Downstream of N2 Vanes (m/s)
V_{a3}	Mixed-mean Axial Velocity of Main Air in Annulus Immediately Downstream of B2 Blades (m/s)
v	Axial Velocity of Main Air in the Annulus (m/s)
α_3	Angle of the Main Air Absolute Velocity, with the Axial Flow Direction, Immediately Downstream of B2 Blade Trailing Edge (◦)
β_2	Angle of the Main Air Velocity Relative to the Blade, with the Axial Flow Direction, Immediately Downstream of N2 Vane Trailing Edge (◦)
η	Time-Averaged Sealing Effectiveness
ρ	Density of Air (kg/m^3)

Ω	Rotor Disk Rotational Speed (rad/s)
μ	Dynamic Viscosity of Air (kg/m-s)

Subscripts

a	Aft Disk Cavity
egress	Egress Air
f	Front Disk Cavity
ing	Ingested Air
inner	Inner Cavity
main	Main Air
purge	Purge Air
rim	Rim Cavity

Abbreviations

CFD	Computational Fluid Dynamics
cfm	Cubic Feet Per Minute
DAQ	Data Acquisition
d/s	Downstream
LE	Leading Edge
rpm	Revolutions Per Minute
TE	Trailing Edge
u/s	Upstream

CHAPTER 1

INTRODUCTION

1.1 Background

A gas turbine is an internal combustion engine which works on the Brayton cycle and uses air as the working fluid. The three main components of a gas turbine are: compressor, combustion chamber and turbine.

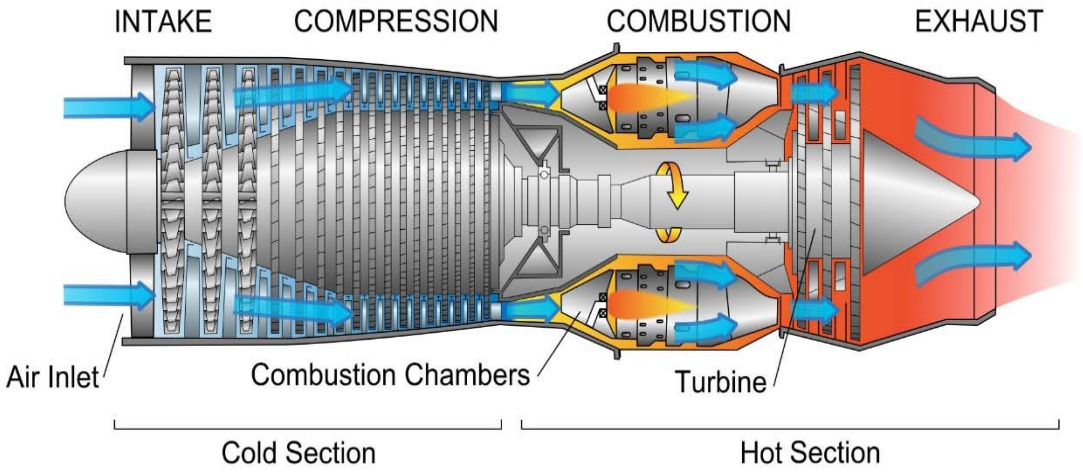

Fig. 1.1 Schematic of a Turbojet Engine [1]

In an axial gas turbine, the air drawn parallel to the axis of turbine rotation, gets incrementally compressed as it passes through multiple compressor stages of alternate rotating (rotor) and stationary blades (stator), thereby increasing the temperature and pressure of the air. The compressed air passes into the combustion chamber where it is mixed with the injected fuel and burnt at a high temperature (~1500 K). This high pressure/temperature combusted air (main gas) expands across the turbine section, which extracts energy from the air. Part of this energy is used to drive the compressor. The excess energy is used either to generate thrust or power, depending on the application.

Increasing the compressor pressure ratio and the turbine entry temperature (TET) increases the thermal efficiency of a gas turbine. Efficient cooling techniques and usage of advanced materials for the components of the turbine has provided the leverage to increase TET over the years. This high temperature, high pressure main gas tends to get ingested into the rotor-stator disk cavities. Two major mechanisms influence this ingestion process: (i) rotationally-induced (RI) ingestion is caused by the rotation of the rotor; centrifugal forces due to the rotor rotation drives the disk cavity fluid radially outward along the rotor wall (disk pumping); to conserve mass, main gas from the annulus is ingested into the cavity – the ingested gas flows along the stator boundary layer before being entrained by the rotor; (ii) externally-induced (EI) ingestion is caused by the circumferential pressure asymmetry in the main annulus that is created by the vane-blade interaction, resulting in the generation of local areas in the main annulus with static pressure higher/lower than the pressure in the disk cavity. The areas with higher static pressure in the annulus result in the ingestion of main gas from the annulus into the cavity, whereas areas with lower static pressure in the annulus result in egress of air from the cavity to the annulus.

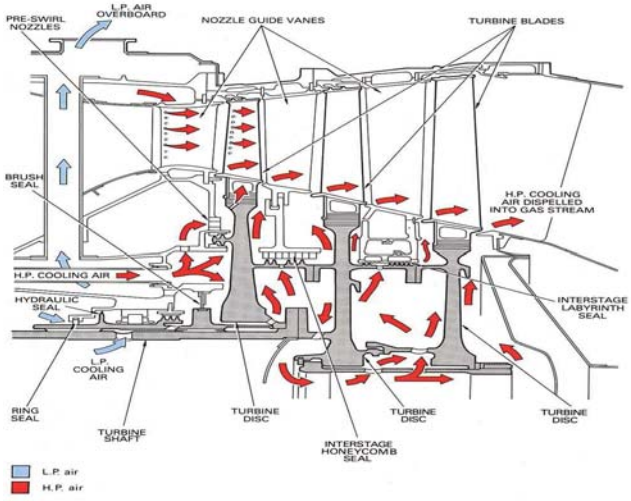

Fig. 1.2 A Hypothetical Turbine Cooling and Sealing Arrangement [2]

Ingestion of main gas into disk cavities must be prevented as much as possible, in order to ensure high lifetime, durability and integrity of the turbine disks. To counter ingestion into the cavities, rim seals are installed on the periphery of the rotor and stator disk. Also, cooler purge air extracted from the compressor discharge is used to pressurize the disk cavities; thereby reducing ingestion and aiding in disk cooling. This however, inflicts a penalty on the turbine efficiency and specific fuel consumption. As such, this purge air flow must be reduced to the extent possible. To better estimate the optimal value of purge air flow rate, a good understanding of the flow field in the main gas path and the disk cavities is essential.

1.2 Literature Review

Over the last few decades, many experimental and computational works have been carried out by researchers to understand the factors that influence the ingestion of main gas into axial gas turbine disk cavities. Some of the important works are discussed briefly in the following.

Batchelor [3] proposed a model to describe the fluid flow field in a rotor-stator disk cavity. According to the model, separate boundary layers exist on the rotor and stator surfaces and a core of fluid rotates in between the stator and rotor at an angular velocity ranging from 0 to the disk rotational speed Ω. Due to disk pumping, ingested air flows radially inward in the stator boundary layer and migrates to the core. The fluid is then entrained from the core by the rotor boundary layer which flows radially outward. The model is depicted in Fig. 1.3.

Daily and Nece [4] studied, both experimentally and theoretically, the flow field associated with the rotation of a smooth plane disk enclosed in a right cylindrical chamber.

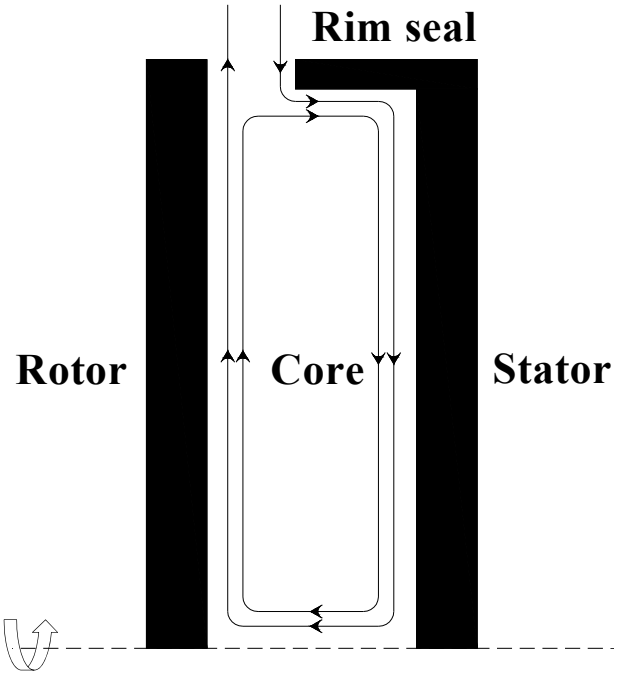

Fig. 1.3 Batchelor's Model for Fluid Flow in a Rotor-Stator Disk Cavity (Open to Quiescent Atmosphere)

Four flow regimes, governed by the rotational Reynolds number and axial gap ratio (G) between the disks, were identified:

Regime I Laminar flow with merged boundary layers and small gap ratio.

Regime II Laminar flow with separate boundary layers and large gap ratio.

Regime III Turbulent flow with merged boundary layers and small gap ratio.

Regime IV Turbulent flow with separate boundary layers and large gap ratio.

Bayley and Owen [5] conducted experiments to study the effect of disk pumping on fluid flow in a shrouded stator-rotor system with superimposed radial outflow in a quiescent environment. It was reported that the minimum dimensionless purge air mass flow rate required to prevent ingestion of air from the quiscent surroundings into the disk cavity was proportional to the rotational Reynolds number and shroud clearance ratio. The stator-rotor axial gap had very little influence on the minimum purge air flow rate.

Phadke and Owen [6] conducted experiments with no external flow to compare various rim seal configurations (one axial clearance seal and four radial clearance seals). The radial clearance seals with a stationary shroud overlapping the rotor showed a "pressure-inversion effect" where the cavity pressure levels increased instead of decreasing with increasing rotational Reynolds number. This effect became larger with increasing purge air flow rate and was the strongest when the degree of overlap of the radial-clearance seals was the highest. Also, the amount of purge air required to prevent ingestion decreased with increasing overlap. The variation of $c_{w,min}$ with Re_ϕ for all of the configurations was compared for three seal clearance ratios. The radial-clearance seal with the greatest overlap was superior for all clearance ratios tested.

Dring et al. [7] realized that the blade-vane spacing had a significant role in driving ingestion into the disk cavity. The periodic unsteady pressure fluctuations from the vane and blade interaction could be large enough to drive rim seal ingestion. These fluctuations decreased as the axial spacing between the vanes and blades was increased.

Phadke and Owen [8]-[10] published a three-part paper to provide insight into the performance of various shroud geometries with and without external flow. Seven different shroud geometries (Fig. 1.4) without vanes and blades were compared for the following external flow conditions: (i) quiescent environment, (ii) quasi-axisymmetric external flow, and (iii) non-axisymmetric circumferential pressure distribution in the main annulus. It is to be noted that seal 4a had no axial overlap whereas seal 4b had an axial overlap.

In the part-I paper, pressure measurement, concentration measurement and flow visualization techniques were used to study the flow structure and performance of the various seals in a quiescent environment. The most effective seals were 4b, 5, 7 and all

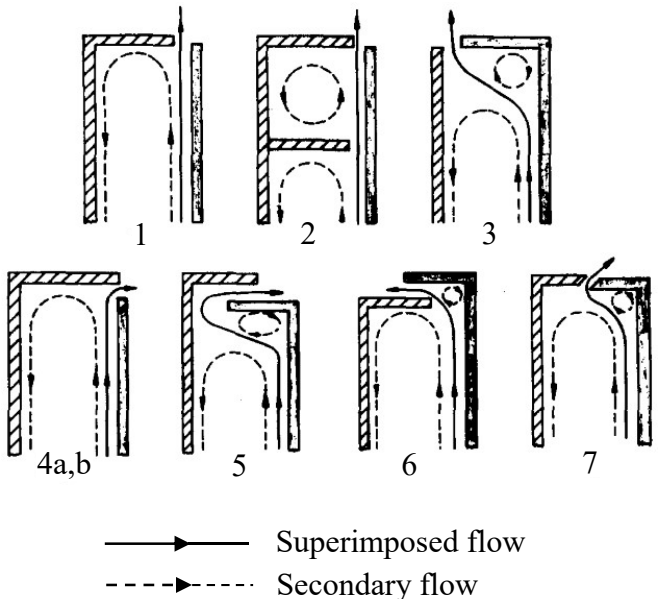

Fig. 1.4 Simplified Representation of Flow Patterns Near the Outlet of Each of the Seven Seals [8]

exhibited a pressure-inversion effect i.e. cavity pressure increased with rotor rotational speed above a certain purge air flow rate, due to the formation of a curtain of fluid in the outer part of the wheel space which increased the cavity pressure, thereby reducing the effective seal clearance and subsequently ingestion. Seal 4b required the least sealing air. A correlation was established between $c_{w,min,}$ G_c and Re_ϕ for all rim-seal geometries:

$$c_{w,\min} \propto G_c^m Re_\varphi^n \quad \textbf{(1.1)}$$

where, m,n are constants obtained from multiple-regression analysis based on minimizing the least-square errors for each seal.

In part II, seals 1, 3 and 5 were compared in a quasi-axisymmetric external flow condition. There was always a misalignment in the annulus; thereby a complete axisymmetric flow could not be achieved. It was found that for all the seals there were two

regimes: rotor rotation-dominated regime at small values of Re_{R_h}/ Re_{ϕ} ($c_{w,min}$ is proportional to Re_{ϕ}), and external flow-dominated regime at large values of Re_{R_h}/ Re_{ϕ} ($c_{w,min}$ independent of Re_{ϕ}). This was in agreement with Abe et al. [11] who observed that for external flow Reynolds number ranging from 3×10^5 to 1×10^6, the effect of the rotating disk on the ingestion of main gas into the disk cavity was negligible.

In part III, the effect of non-axisymmetric external flow on ingestion is considered. Seals 1, 2, 3 and 5 are compared in this part. A correlation was established between $c_{w,min}$, G_c, and P_{max}:

$$c_{w,min} = 2\pi K G_c P_{max}^{0.5} \quad (1.2)$$

where, K - empirical constant

P_{max} - $0.5 C_{p,max} Re_{R_h}^2$

$C_{p,max}$ - non-dimensional maximum circumferential pressure difference in annulus.

Using this correlation and the correlation for rotationally-dominated ingestion discussed in Part I, a conservative estimate of $c_{w,min}$ could be obtained. It was observed that seal 2 with a double-shrouded radial clearance had a better sealing performance over the other seals as flow visualization indicated that the outer wheelspace of the seal acted as a ring road that transported most of the ingested fluid.

Dadkhah et al. [12] investigated a rotor-stator system that was easily reversible to test wheelspaces upstream and downstream of the rotor. The performance of two radial clearance seals: (i) upward rotor lip upstream of the rotor, and (ii) upward stator lip downstream of the rotor, were analyzed in a nominally axisymmetric external flow. Axial distribution of tracer gas concentration for both the wheelspaces showed that the purge air

dilution by external air was more evident near the stator than near the rotor, and the outer radii was the most diluted. The interaction of sealing flow with the mainstream flow was important in influencing ingestion. $c_{w,min}$ estimated from pressure measurements indicated that the seal upstream of rotor performed better than the seal downstream of rotor, but concentration measurement showed that for $c_w < c_{w,min}$, the level of ingestion was more for the upstream seal.

Johnson et al. [13] reported the physical mechanisms important to the rim seal ingestion process.The mechanisms were (i) disk pumping, (ii) periodic vane/blade pressure field, (iii) three-dimensional geometry in the rim seal region, (iv) asymmetries in the rim seal geometry, (v) turbulent transport in the platform overlap region, (vi) flow entrainment.

Bohn et al. [14] investigated experimentally and numerically ingestion in a rotor-stator system with guide vanes but no blades with external flow. Velocity measurements using a two-dimensional laser doppler velocimetry (LDV) system showed that radial outflow was closer to the rotor, and ingestion of main air was near the stator. It was pointed out that main gas ingestion can occur on the rotor side of the wheelspace as well.

Green and Turner [15] performed experiments in a complete stage featuring vanes and blades as well as an axial clearance rim seal. Sealing effectiveness for the wheelspace with the axial clearance seal was compared for the following four external flow conditions: (i) no external flow, (ii) axisymmetric external flow, (iii) vanes only and (iv) complete stage with vanes and blades. The condition with no external flow showed least ingestion, and the condition with vanes only showed maximum ingestion. Surprisingly, the condition with the complete stage showed a level of ingestion closer to the no external flow condition. It appeared that the rotor blades had the effect of smoothening out the vane pressure

asymmetry. It was also observed that a certain amount of ingestion was always present in the complete stage irrespective of the supply of high purge flow.

Roy et al. [16] conducted experiments in a subscale single-stage turbine with vanes and blades to measure time-averaged and unsteady pressure fields as well as the velocity field in the main gas path and disk cavity. The concentration measurements showed ingestion that three-dimensional steady simulations failed to predict. Unsteady pressure field due to vane/blade interaction was identified as one of the causes of main gas ingestion. It was suggested that a three-dimesnsional unsteady simulation of the main gas and disk cavity flows could correctly predict ingestion.

Roy et al. [17]-[22] employed experimental techniques such as time-averaged static pressure measurement, unsteady static pressure measurement, tracer gas concentration measurement, and PIV (Particle Image Velocimetry) to examine various rim seal geometries. The aim was to get a better understanding of flow fields in the main gas path and disk cavity to characterize ingestion through various rim seal geometries and study the interaction of cavity egress air with the mains air.

Narzary et al. [23] investigated the improvement in sealing by a double rim seal over a single rim seal. It was observed that the cavity pressure levels followed (increased or decreased) the pressure level in the main gas path. Tracer gas concentration measurements showed a significant improvement in sealing for the double rim seal only at relatively low purge air flow rate. Except for the radially outer one-fifth of the cavity, the single rim seal appeared to perform slightly better.

Bohn et al. [24] conducted unsteady two-dimensional LDV measurements in the upstream cavity of a 1.5-stage turbine featuring 16 vanes (for each row) and 32 blades. The cavity featured a simple axial clearance seal at its rim. Radial and circumferential velocities at dimensionless radii of 0.985 and 0.952 were measured for two purge air flow rates (c_w=10000 and 20000). Measurements near the cavity periphery indicated main gas ingestion to be influenced by both the rotor blades & stator vanes, and ingestion to occur even at high purge flow rates. Also, the location of ingestion moved with the rotor blades and its strength depended on the level of purge air flow rate. The effect of blades and vanes on the disk cavity flow field at radially inboard locations was found to be negligible.

Jakoby et al. [25] carried out CFD simulations to understand main gas ingestion through an axial clearance seal into the upstream disk cavity of a 1.5-stage axial turbine based on Bohn et al.[24]. An unsteady 360° simulation indicated the presence of a large-scale structure within the cavity, which at low purge flows rotated at about 80% of the rotor speed. The rotating structure was found to have considerable influence on main gas ingestion. It was found that increasing the purge air flow rate inhibited these effects.

Bohn et al. [26] conducted experiments in a 1.5-stage axial turbine with vanes and blades. Static pressure measurements and concentration measurements using the tracer gas technique (CO_2) were carried out for the upstream cavity. Two rim seal configurations were investigated: (i) an axial clearance rim seal, (ii) a radial clearance rim seal with an axial overlap. The radial clearance rim seal was found to have better sealing performance.

Johnson et al. [27] formulated a rim seal model using two C_d values, one for ingestion (C_{di}) and one for egress (C_{de}), unlike most of the published rim seal orifice models with a single C_d value for both ingestion and egress. The authors reasoned that the flow from the

main gas path through the rim seal is more convoluted than the flow returning to the main gas path and hence the necessity of two C_d values. Using two C_d values also provided an improved characterization for seals over a wide range of purge air flow rates. The model was evaluated with the experimental results of Roy et al [19]. The difference between the main gas static pressure just above the vane platform lip (this pressure was obtained from a P&W in-house CFD code) and the disk cavity static pressure at 0.9 (blade-vane hub radius) was taken as the pressure differential that drove either ingestion or egress across the rim seal. Best-estimate values of C_{di} and C_{de} were reported; a single value for each coefficient was determined for a range of purge air flow rates.

Balasubramanian et al. [28] carried out experiments in a 1.5-stage (vane-blade-vane) axial flow air turbine to investigate main gas ingestion into the aft disk cavity. The cavity featured a rim seal with radial clearance and axial overlap as well as an inner labyrinth seal which divided the disk cavity into an inner cavity and outer (rim) cavity. Pressure measurements indicated that tangential motion of the cavity fluid caused a radial pressure gradient in the rim cavity. It was observed through concentration measurements (CO_2 tracer gas technique) that the inner cavity was completely sealed at high purge air flow rate but significant ingestion occurred in the rim cavity. Also, ingestion was higher for the experimental conditions with higher mainstream air flow rate and rotor speed at the same purge air flow rate.

Rabs et al. [29] investigated flow instabilities near the rim cavity of a 1.5-stage gas turbine using CFD simulations of a 22.5° sector. The authors reported the conditions for formation of Kelvin-Helmholtz vortices and explained that the conditions are fulfilled in a rim cavity environment. The formation of Kelvin-Helmholtz vortices near the rim was

identified in a simplified model (blades and vanes absent). It was noticed that the vortices became more distinctive at higher purge air flow. The formation of Kelvin-Helmholtz vortices in a full CFD model with vanes and blades was also observed, but their frequency of occurrence was lesser when compared to the sector model, suggesting its suppression due to the presence of vanes and blades. Nevertheless, the Kelvin-Helmholtz vortices influenced the flow field near the rim seal (ingestion at the rotor and egress at the stator).

Luo et al. [30] studied the flow field within the front disk cavity of a 1.5-stage axial turbine, both experimentally and numerically. The turbine featured full span and full length airfoils in each vane row and blade row and a simple axial clearance seal at the cavity periphery. The main gas path was seeded with smoke and the flow field within the cavity was mapped by PIV. A time-dependent CFD simulation was carried out for a sector model of the cavity with one blade and one vane). Both PIV and CFD results indicated regions of ingestion and egress to be present simultaneously near the rim seal at different circumferential locations and rotated with the rotor. The ingested air was found to flow along the stator surface before being entrained into the rotor boundary layer.

Teuber et al [31] proposed a method to extrapolate the sealing effectiveness of an axial clearance seal from test rig to engine conditions using a CFD model. The theoretical model proposed by Owen [32] predicts that the non-dimensional minimum sealing flow (ϕ_{min}) is proportional to $\Delta C_p^{1/2}$. ΔC_p was considered as the main driving force for ingestion through the rim seals.

$$\Delta C_p = \frac{\Delta p}{\frac{1}{2}\rho\Omega^2 b^2} \tag{1.3}$$

where, Δp is the peak-to-trough static pressure difference in the main annulus.

b is the radius of the rim seal.

It was proposed that the values of ϕ_{min} and ΔC_p obtained at incompressible flow conditions in the rig, is quantitatively relevant to a geometrically similar engine operating at a higher Mach number. A relationship was established between the rig and engine, ϕ_{min} and ΔC_p values.

$$\frac{\phi_{min,engine}}{\phi_{min,rig}} = \left(\frac{\Delta C_{p,engine}}{\Delta C_{p,rig}} \right)^{\frac{1}{2}} \tag{1.4}$$

This relationship holds good if ΔC_p is computed at the same location in the main annulus of the rig and engine. This method was tested only for subsonic conditions in the annulus.

Sangan et al. [33]-[35] published a three-part paper for ingestion measurement across turbine rim seals. In part I, two rim seals (a simple axial clearance seal and a generic radial clearance seal) were investigated with external flow. An expression that related the rim seal sealing effectiveness, purge air flow rate, and minimum purge air flow rate, based on an orifice model by Owen [36], was presented. The expression incorporated the ratio C_{di}/C_{de} denoted by Γ_c as a parameter, and was assumed to be constant for a given rim seal configuration. Best-estimate values of Γ_c and minimum purge air flow rate were obtained from ingestion experiments. The peak-to-trough pressure asymmetry amplitude in the main gas annulus at zero purge air flow rate could be used to determine C_{di} and C_{de}. The radial clearance seal performed better in sealing the disk cavity.

In part II, the two rim seals were investigated without an external flow. The aim was to determine the contribution of disk rotation to ingestion. The orifice model was modified for RI ingestion. RI ingestion was compared to EI ingestion for the same Re_ϕ and λ_{turb}. EI ingestion caused much more ingestion.

In part III, the performance of double rim seals was assessed. Four different single rim seals and two different double rim seals were compared. The rim seal with largest axial overlap and smaller radial-clearance performed the best. The double rim seal proved beneficial as the outer wheel-space attenuated the circumferential pressure asymmetry in the mainstream gas, thereby reducing ingestion. It was proposed that if the pressure asymmetry is completely eliminated in the outer wheel-space, EI ingestion would dominate for the outer seal and RI ingestion for the inner seal. Thus the performance limit of a double rim seal is when the inner seal is exposed to RI ingestion.

Bhavnani et al. [37] found that, the more complex the rim seal configuration was, the lesser the cooling flow required. It was concluded that smaller radial clearance with an axial overlap resulted in minimum cooling flow, and that decreasing radial clearance had more effect than increasing the axial overlap. This was evident from the work of Scobie et al. [38] where an improved rim-seal called ‘angel-wing seal’ was designed. The seal exploits the disk pumping effect; the sealing flow from the rotor boundary layer is pumped directly opposing the ingested flow, thereby helping to prevent ingestion. Also, two buffer cavities formed by the seal attenuates the circumferential pressure asymmetry further, thus proving to be highly effective in comparison with a double rim seal. Sangan et al. [39] evaluated the performance of a finned rim seal. The radial fins increased the swirl in the outer wheelspace. Swirl measurements showed that the captive fluid in between the fins rotate

at near solid body rotation. This attenuated the pressure asymmetry and also increased the pressure in the outer wheelspace, thereby reducing ingestion. Though the presence of radial fins improved the sealing performance, encouraging swirl in the outer wheelspace increased windage on the rotor reducing the stage efficiency.

1.3 Overview of Present Work

In the present work, experiments were conducted in a subscale 1.5-stage axial flow air turbine featuring vanes and blades. The disk cavity upstream of the rotor is designated as the 'front cavity' and the disk cavity downstream of the rotor, the 'aft cavity'. An axially-overlapping radial clearance double seal was present at the front cavity rim while an axial clearance double seal was present in the aft cavity. Labyrinth seals were provided radially inboard for both the front and aft cavities; this seal divided each disk cavity into an 'inner cavity' and a 'rim cavity'.

The remainder of the thesis is organized as follows:

Chapter 2: describes the experimental facility, the 1.5-stage turbine test section, the experiment procedures and the measurement locations. It also describes the components that were used for measurement during the experiments.

Chapter 3: contains experimental results and their discussion.

Chapter 4: summarizes the conclusions of this study.

CHAPTER 2

EXPERIMENTS

2.1 Experimental Facility

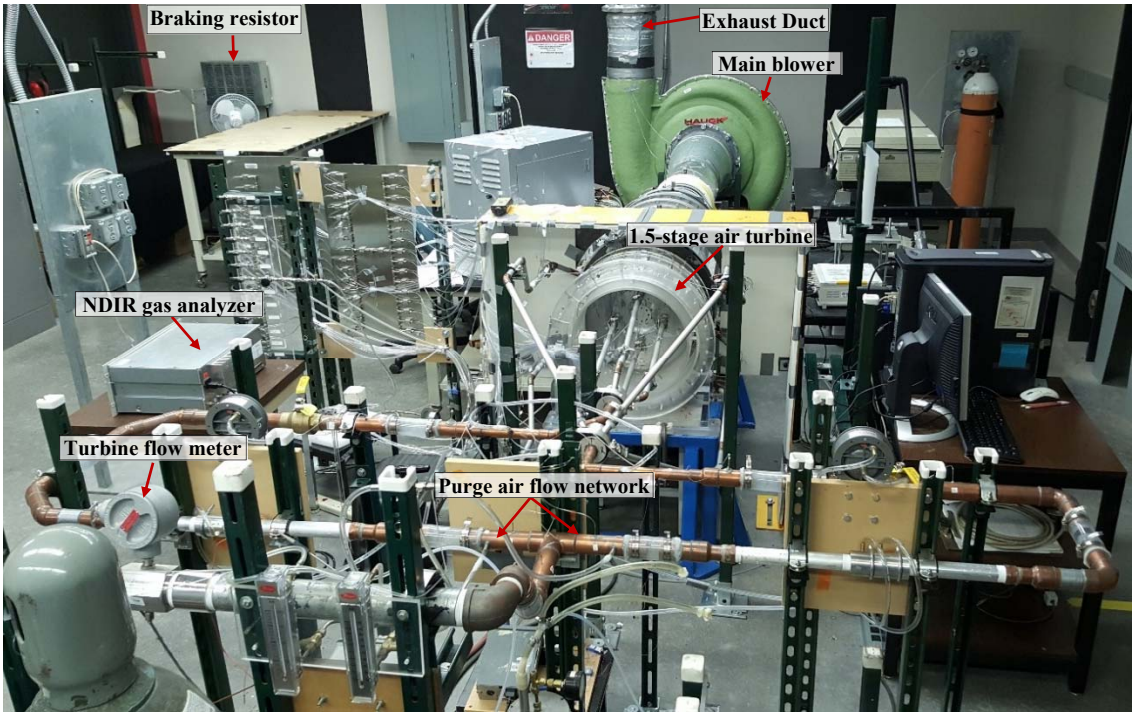

Fig. 2.1 Experiment Facility

Figures 2.1, 2.2 and 2.3 show the experimental facility which was used for this work. The three major components of the facility, viz, the 'main blower', 'secondary blower' and the 'rotor driving system' are explained below.

Main Blower

The 1.5-stage axial air turbine is located on the suction side of a centrifugal blower (22.4 kW, HAUCK, TBA-20-30) which has an inlet diameter of 412.75 mm (16.25") and can draw air up to 1.42 m^3/s (~3000 cfm) at 100% motor rating. The main blower's operation is controlled by a variable frequency drive (VFD) (Cutler Eaton AF-95).

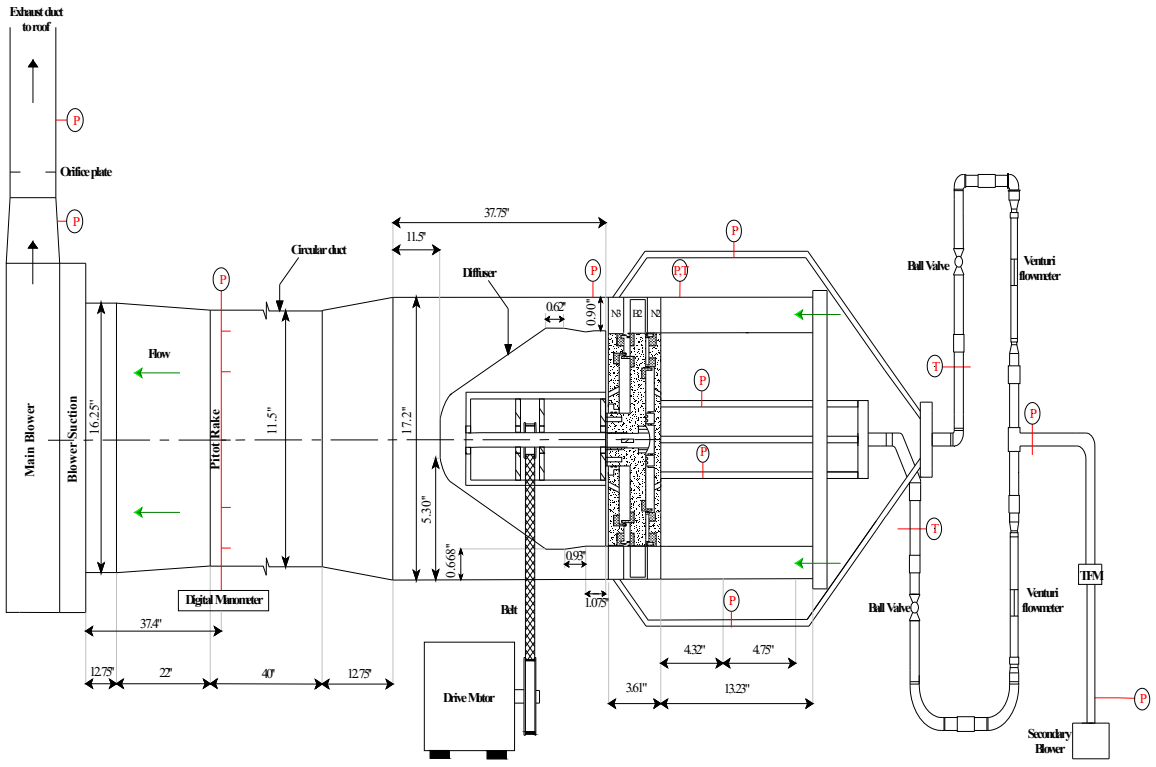

Fig. 2.2 Schematic of ASU Turbine Test Rig

The blower is connected to a plexiglass circular duct (as shown in Fig. 2.3) of diameter 292.1 mm (11.5”) via a diffuser with divergence angle of 5°. This circular duct houses the pitot tube rake used for main air flow measurement. A 311 mm (12.25”) inner diameter, vertical pipe connects the outlet of the blower to the atmosphere via an exhaust duct on the building roof.

The main air flow pressure drop through the rig was such that the blower operated in the stall regime. To overcome this, an opening (about 33% of circumference, as shown in Fig. 2.3) was created at the inlet to the blower, so that adequate in-leakage of air occurred, thereby stabilizing the blower operation.

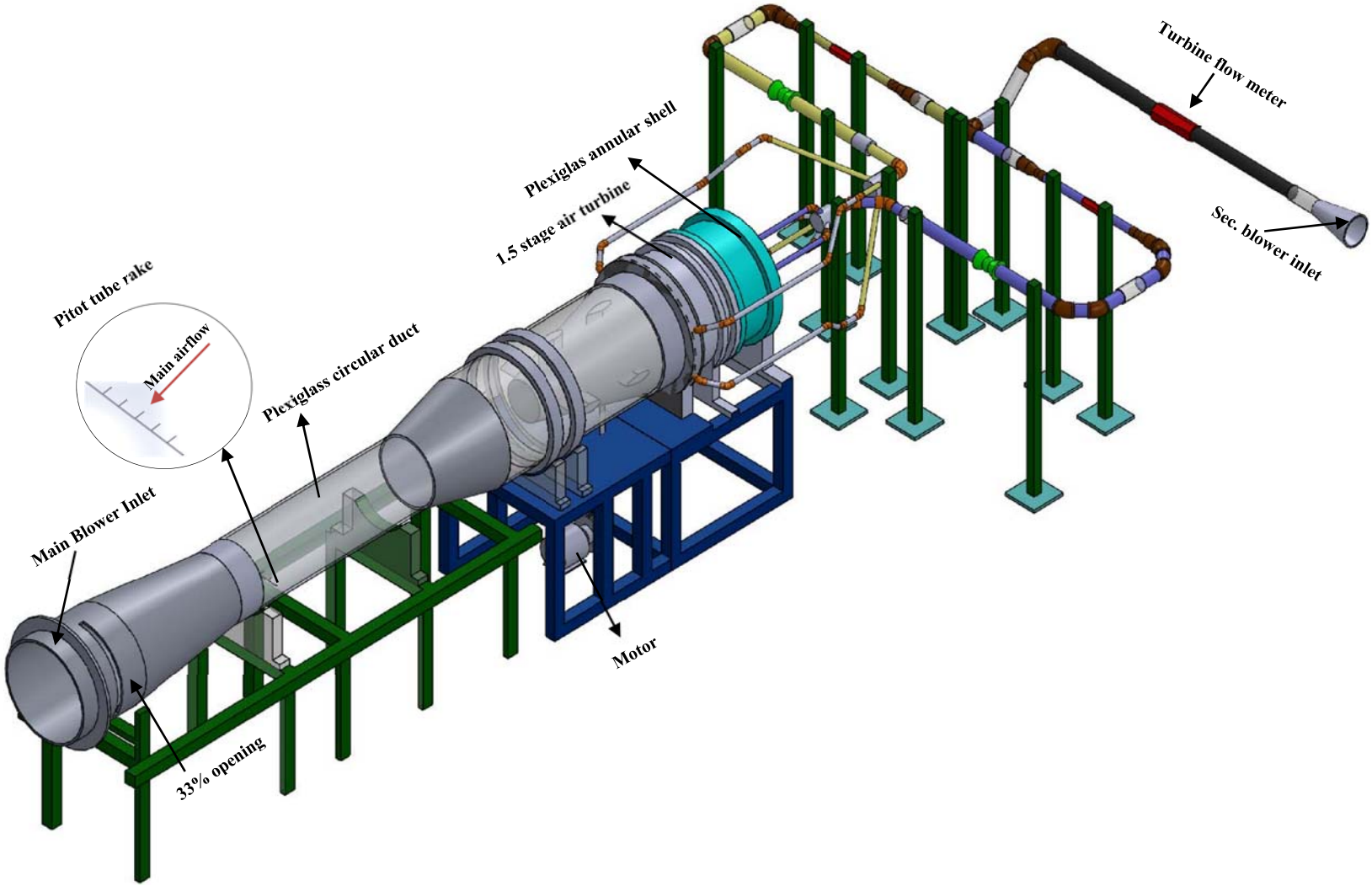

Fig. 2.3 Three-dimensional Model of ASU Experiment Test Rig-Isometric

Main air flow rate measurement

A pitot tube rake (United Sensor, UNSH-N-107) equipped with five pitot-static tubes spaced equally along a manifold is installed in the plexiglass circular duct (Fig. 2.3) at 2.23 m (7'4") downstream of the test section. The rake was connected to a digital manometer (Validyne PS309, 0-2" H_2O) which measures the dynamic head (thereby the flow rate) of the air flowing in the plexiglass duct.

$$P_{dynamic} = P_{stagnation} - P_{static} = 0.5\ \rho v^2 \quad (2.1)$$

$$\text{Flowrate, } Q = \text{Area}_{duct} \times \left(\frac{2 \times P_{dynamic}}{\rho} \right)^{0.5} \quad (2.2)$$

The manometer provides an analog output (0-2 V, 0.25% accuracy full scale) corresponding to the measured dynamic head. The analog output was routed to the NI-USB 6009 DAQ card and was sampled at 5 kHz for 20 seconds using LabVIEW.

Secondary Blower

The purge air was supplied by a smaller centrifugal blower (2.24 kW, HAUCK, TBA-16-3), which was controlled by a VFD (4.84 kW, Prism, Emerson Controls). The blower can supply purge air up to 0.12 m^3/s (250 cfm) at 100 % motor rating. A galvanized iron (G.I.) pipe of length 1.67 m (5'6") and diameter 50.8 mm (2") was connected to the discharge of the blower. At a distance of 1.07 m (3'6") from the blower discharge, a turbine flow meter (EG&G Flow Technology, FT-32, uncertainty of ±0.2% of the displayed value) was installed to measure the discharged flow from the blower. The turbine flow meter sends an analog output to a digital multi-meter (Fluke 45). From a known calibration chart, the corresponding flow rate for this measured output voltage was obtained. The analog output was routed to the DAQ card for sampling.

Purge Air Flow Network

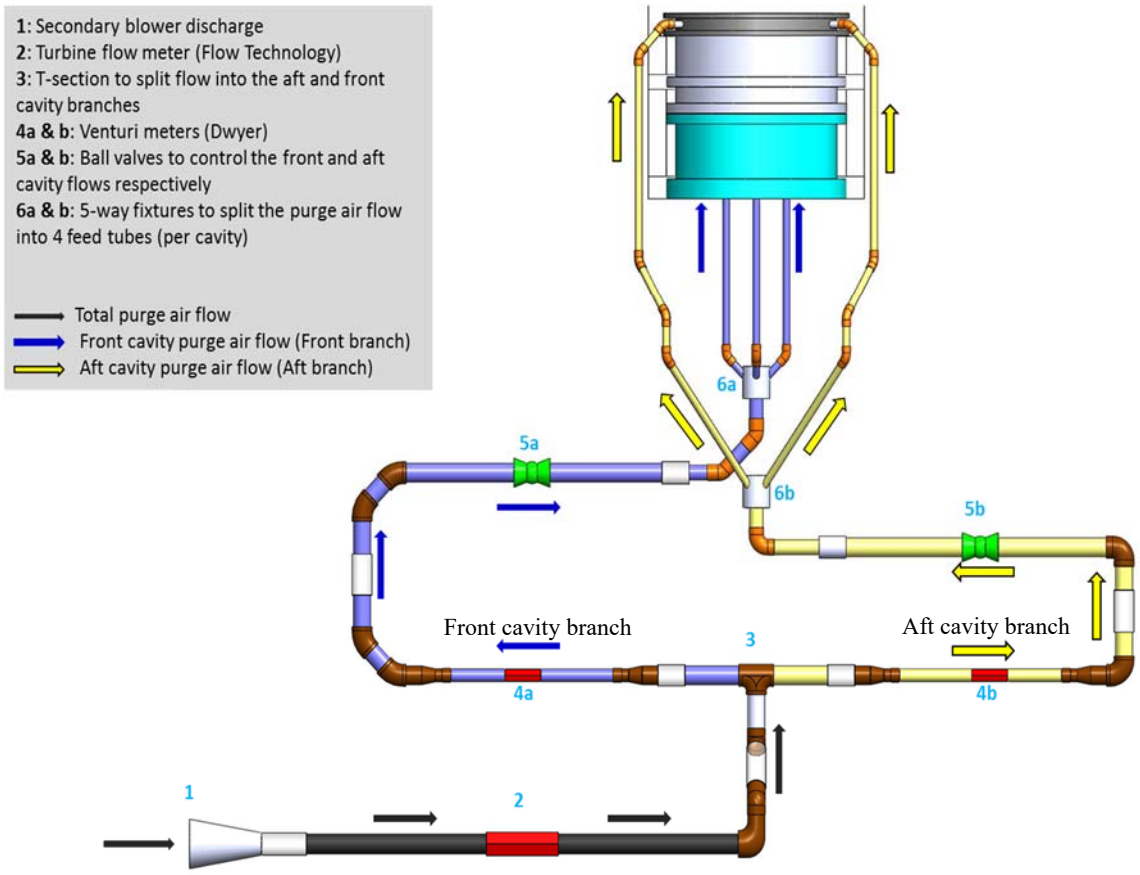

Fig. 2.4 Schematic of Purge Air Flow Distribution Network–Top View

The G.I. pipe connects the blower discharge to a T-section which divides the purge air flow network into two branches (as shown in Fig 2.4) – the 'front cavity branch' and the 'aft cavity branch' corresponding to the front (upstream of rotor) and aft (downstream of rotor) disk cavities, respectively. Each branch was split further into four 'feed tubes' that discharge into a manifold, feeding the associated disk cavity via eight feed holes equally spaced circumferentially on the stator. The purge air flow rate through each branch is measured by a venturi flow meter (Dwyer, 2000-20VF1) and is controlled by ball valves.

Rotor Driving System

The rotor was mounted on a mild-steel shaft of diameter 50.8 mm (2") which was belt-driven by a 2.24 kW (3HP) GE motor. The step-up belt drive has a speed ratio of 3.27:1 yielding a maximum rotor speed of 5722 rpm. The motor was controlled by a variable frequency drive (5 HP, Eaton Cutler-Hammer SVX9000) which maintains the rotor at a particular speed during the experiments. A digital photoelectric handheld tachometer (Biddle Instruments, accuracy ±1 rpm) was used to measure the rotational speed of the motor.

During the rig operation, the motor acts as a generator due to the energy input from the main air flow. This excess energy is transferred to a capacitor in the VFD and is subsequently dissipated as heat across a braking resistor (Power-Ohm Resistors, P13549-405, rated at 2.8 kW at a total resistance of 65.0Ω).

2.1.1 1.5-stage Turbine Test Section

The experiments were conducted in a newly constructed subscale 1.5-stage axial flow air turbine (Fig.2.5). The stage design and airfoil geometries are based on an actual gas turbine of Solar Turbine Inc. The turbine dimensions were scaled down to fit the lab's existing rig dimensions. The model 1.5-stage turbine features an upstream stator (N2), rotor (B2) and downstream stator (N3). The stator-rotor-stator spacings mimic the scaled down dimensions of Solar Turbine's gas turbine during hot running conditions.

In the test section, main air is drawn through a plexiglass annular shell (Fig. 2.3) in which the upstream stator (N2) is housed. The aluminum stator is 405.4 mm (15.96") in diameter and has 40 partial height, full length vanes which turn the incoming flow at an angle of 69.8˚to the axial direction, thereby imparting a realistic swirl to the air.

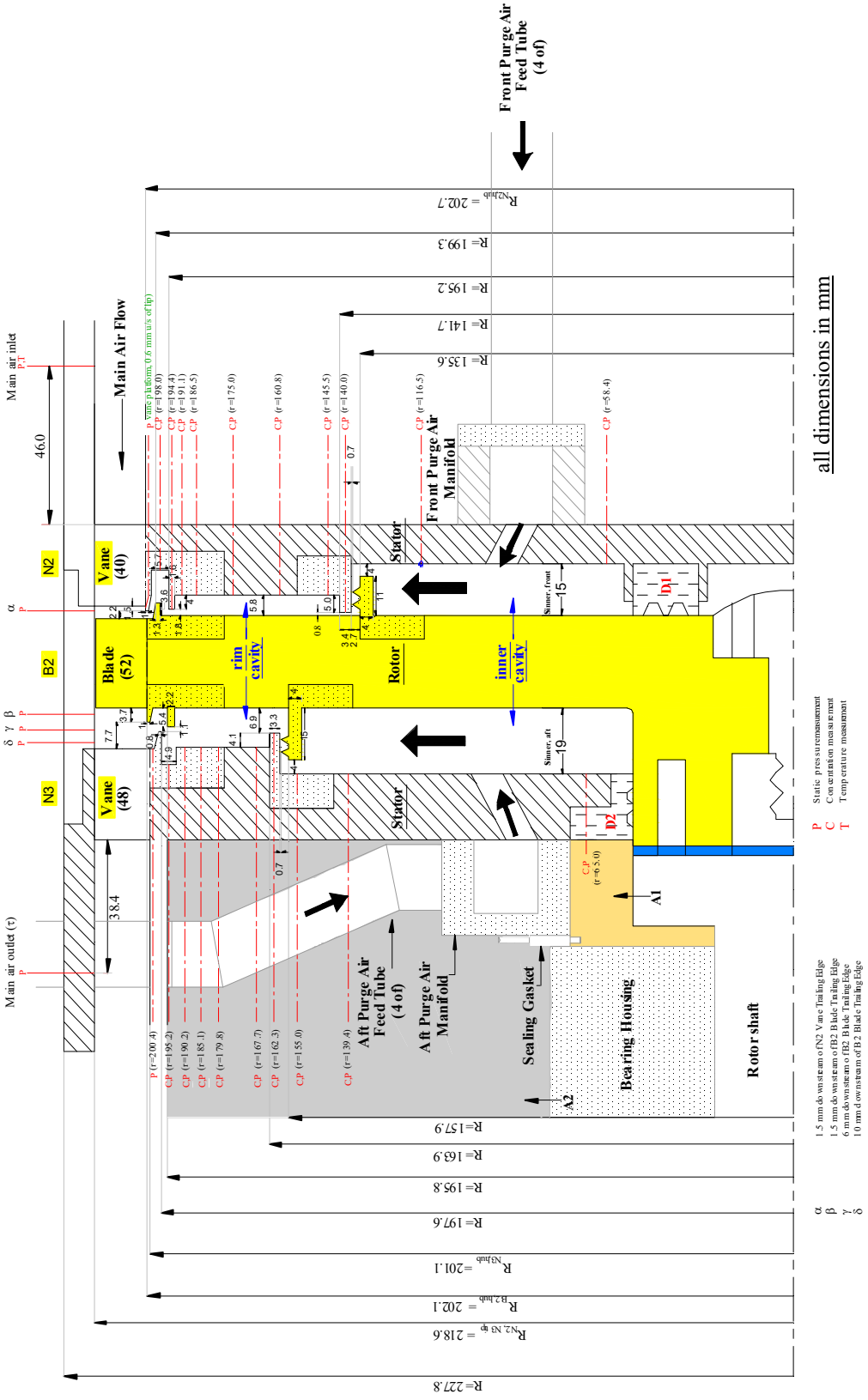

Fig. 2.5 Schematic of 1.5-Stage Axial Flow Air Turbine

The aluminum rotor (B2) of diameter 404.2 mm (15.91”) is equipped with 52 partial height, full length blades. It has a blade tip clearance of 0.75 mm with the outer shroud. The aluminum stator (N3) downstream of the rotor is of diameter 402.2 mm (15.83”) and is equipped with 48 partial height, full length vanes. The vane and blade heights are such that for a given main blower capacity, sufficiently high main air axial velocity in the annulus can be obtained so as to result in an acceptable velocity triangle upstream of the blade row at prescribed rotor speeds. Table 2.1 lists the salient airfoil features.

Table 2.1 Salient Features of the Vanes and Blades

N2 stator	
Vane angle (α_2)	69.8°
Vane height	15.9 mm
Vane axial chord length	23.4 mm
Hub radius	202.7 mm
B2 rotor	
Blade angle (β_3)	66.5°
Blade height	15.7 mm
Blade axial chord length	26.3 mm
Hub radius	202.1 mm
N3 stator	
Vane angle (α_4)	64.5°
Vane height	17.5 mm
Vane axial chord length	26.7 mm
Hub radius	201.1 mm

The vanes and blade shapes, arrangement and the resulting velocity triangles are shown in Fig. 2.6. β_2 is the angle of the main air velocity relative to the blade (W_2) with respect to the axial direction. A large positive value of β_2 ensures that the rotor operates as a turbine. It is assumed that the velocity triangles shown below are undisturbed by the purge

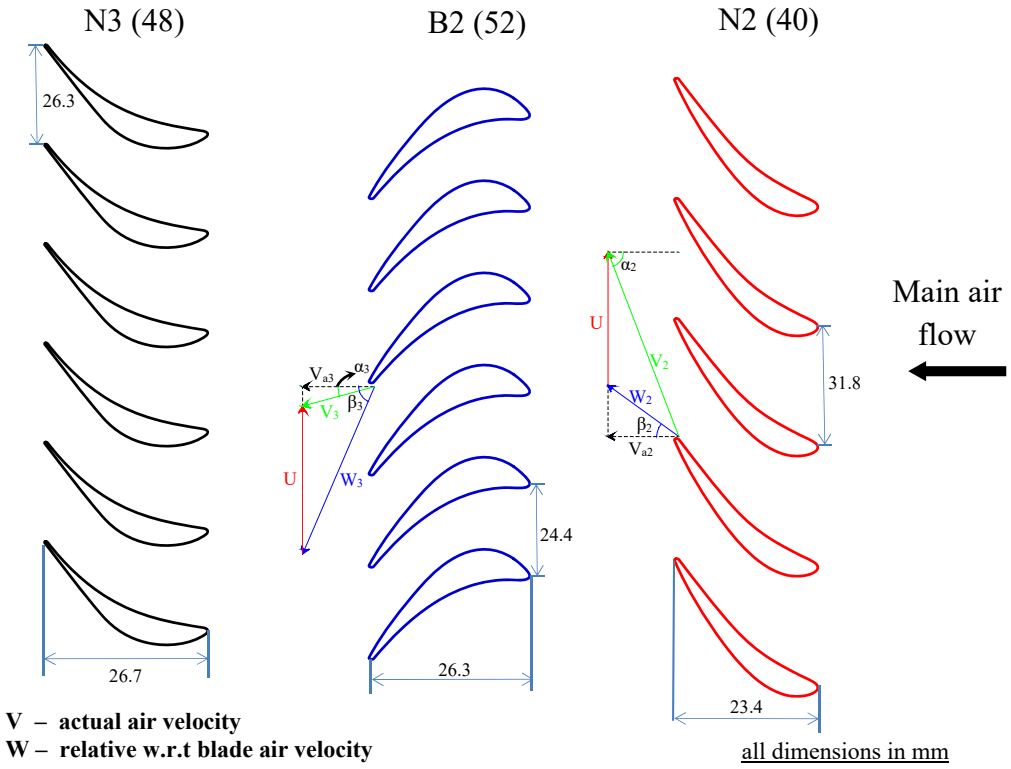

Fig. 2.6 Main Air Velocity Triangles –Immediately Downstream of N2 Vanes and B2 Blades

air flow as the maximum ratio of purge air flow to main air flow is very small. It is to be noted that the vane-blade axial spacings in Fig.2.6 are not to scale.

Rotor-stator disk cavity

As stated earlier, the front disk cavity is upstream of the rotor and the aft disk cavity is downstream of the rotor. Both the cavities incorporate a labyrinth seal radially inboard (radial clearance=0.7 mm); which divides the disk cavity into an inner cavity (radially inboard) and a rim cavity (radially outboard). It is to be noted that for both the disk cavities, the cavity axial gap is different in the rim cavity and inner cavity. The stator-rotor-stator spacing are such that the front disk cavity double rim seal has an axial overlap whereas the aft disk cavity double rim seal has an axial clearance.

Front disk cavity

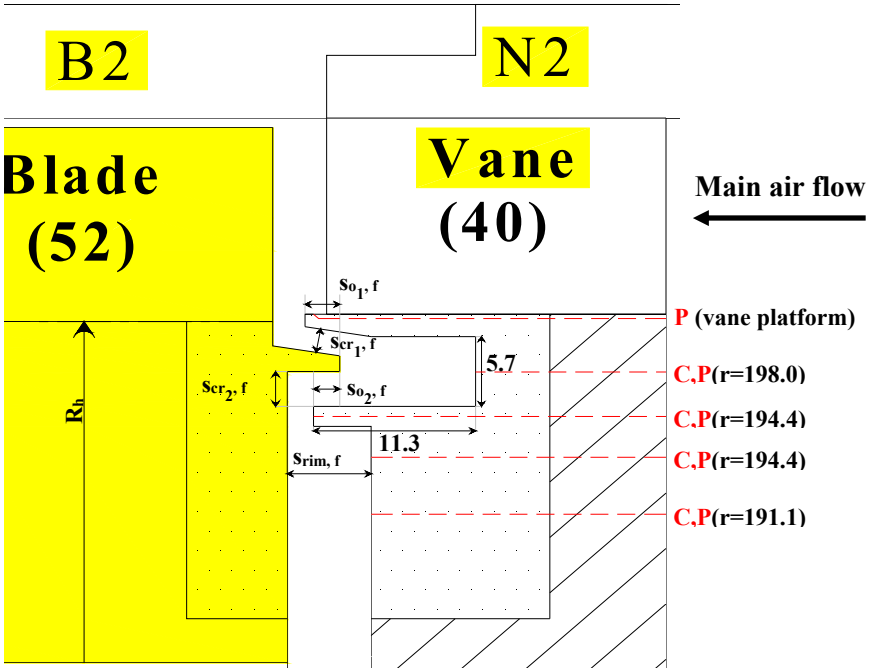

Fig. 2.7 Front Disk Cavity- Rim Seal Geometry

The front disk cavity has an axially overlapping radial clearance double rim seal with a recess (as shown in Fig. 2.7) on the N2 stator surface. Table 2.2 lists the important gaps/dimensions of the front disk cavity.

Table 2.2 Salient Features of Rim Seal and Cavity (Front Cavity)

$s_{o_1,\,f}$ (rim seal axial overlap 1)	2.4 mm
$s_{o_2,\,f}$ (rim seal axial overlap 2)	1.8 mm
$s_{cr_1,\,f}$ (rim seal radial clearance 1)	1.9 mm
$s_{cr_2,\,f}$ (rim seal radial clearance 2)	2.8 mm
$s_{rim,\,f}$ (rim cavity gap)	5.8 mm
$s_{inner,f}$ (inner cavity gap, Fig. 2.5)	15.0 mm
R_h (Rotor hub radius)	202.1 mm
$G_{cr,f}$ ($s_{cr_1,\,f}/R_h$)	0.0095
$G_{rim,f}$($s_{rim,\,f}/R_h$)	0.0288

Aft disk cavity

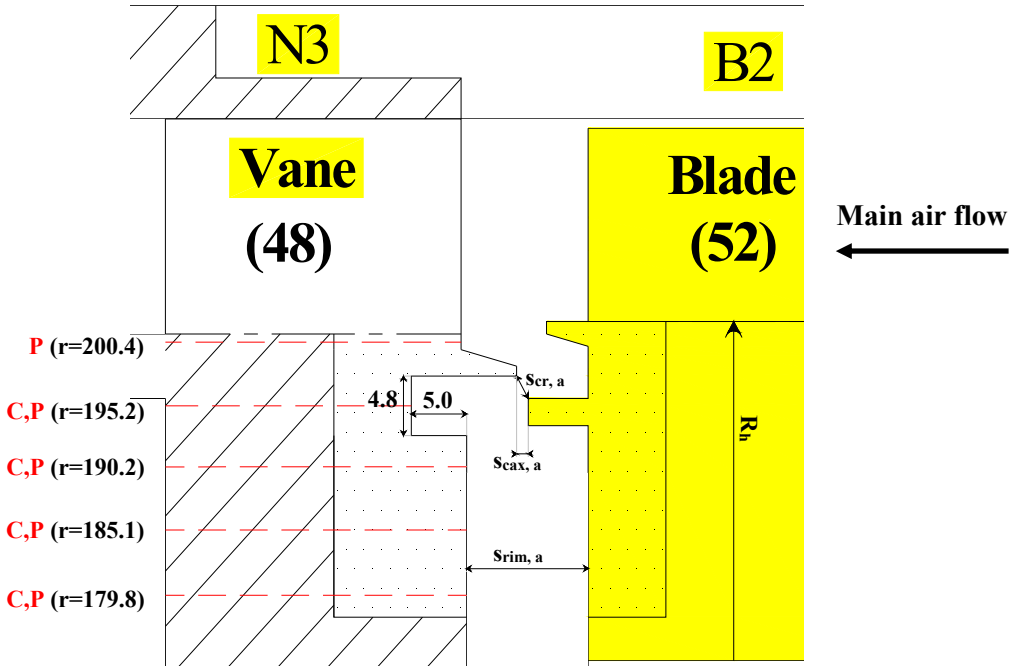

Fig. 2.8 Aft Disk Cavity- Rim Seal Geometry

The aft cavity has an axial clearance double rim seal with a recess (as shown in Fig. 2.8) on the N3 stator surface. Table 2.3 lists the important gaps/dimensions of the aft disk cavity.

Table 2.3 Salient Features of Rim Seal and Cavity (Aft Cavity)

$s_{cr,\,a}$ (rim seal radial clearance)	2.1 mm
$s_{cax,\,a}$(rim seal axial clearance)	1.1 mm
$s_{rim,\,a}$ (rim cavity gap)	10.9 mm
$s_{inner,a}$ (inner cavity gap, Fig. 2.5)	19.0 mm
R_h (Rotor hub radius)	202.1 mm
$G_{cr,a}$ ($s_{cr,\,a}/R_h$)	0.0104
$G_{rim,a}$($s_{rim,\,a}/R_h$)	0.0542

For both the cavities, the associated purge air manifold feeds eight feed holes of diameter 8.9 mm (0.35”) equally spaced on the corresponding stator surface. Each feed hole has a rectangular cross-section (8.9 mm×10.2 mm) on the cavity side and is at an angle of 30° to the stage axis. The rectangular cross-section of the feed holes and angular feeding were used for better distribution of the purge air in the inner cavity and for enhanced mixing of the tracer gas (CO_2) inside the inner cavity during concentration measurements.

Figure 2.5 shows Delrin seals that were installed on the N2 stator (D1) and at the N3 stator interface with the rotor hub (D2). After initial run of the test section, leakage of aft disk cavity purge air (into the region behind N3 stator) was found to occur through the radial clearance gap between the Delrin seal (D2) and rotor hub (detected by tracer gas concentration measurements, discussed later in this thesis). To counter this leakage and provide sealing, a gasket was sandwiched between the bearing housing and aft purge air manifold resulting in the formation of a buffer cavity (A1, as shown in Fig 2.5) which contained the leaked air from leaking into the region A2 (outside the buffer cavity A1). The cavity A1 is now a part of the aft disk cavity. The time-averaged static pressures (discussed later in this thesis) and concentrations were measured within locations A1 and A2 for all experiments to ensure no leakage of air occurred from A1 to A2.

Figure 2.5 also shows a spacer ring (shown in blue color) of thickness 3.5 mm (0.138”) which was installed between the rotor hub and the spindle of the driving shaft. This was used to enable the shifting of the rotor axially by 3.5 mm towards the N3 stator to study the effects of cavity gaps and rim seal overlaps on main gas ingestion.

2.2 Time-averaged Static Gage Pressure Measurement:

The time-averaged static pressure is defined as

$$\overline{p} = \frac{1}{T}\int_0^T p(t)dt \approx \frac{1}{N}\sum_{i=1}^{N} p_i \qquad (2.3)$$

where, N is the number of samples collected over a time period T.

2.2.1 System Components

The static pressure measuring system consists of the following components:

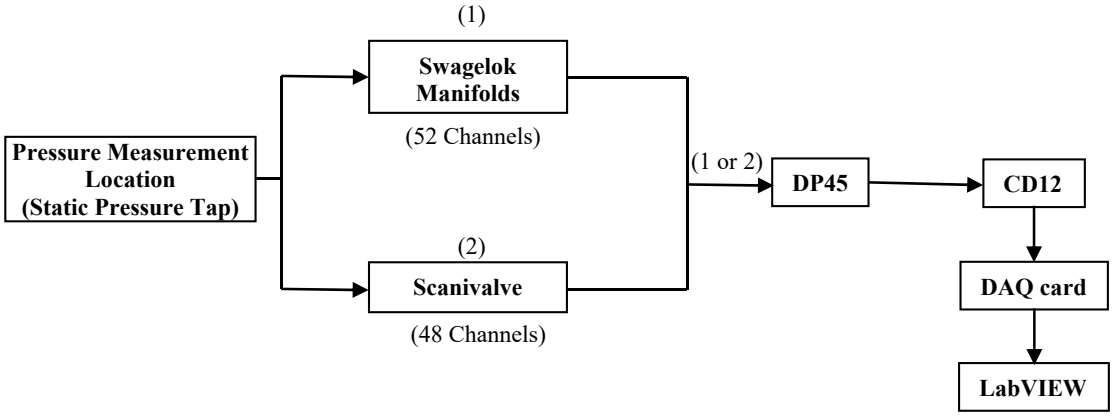

Fig. 2.9 Schematic of the Static Pressure Measurement System

The Scanivalve (48 channel)-Swagelok manifolds (52 channel) combination was used to sequentially connect the different pressure ports to the pressure transducer DP45. The transducer output was routed to the pressure signal carrier demodulator (CD12) which in turn was routed to the data acquisition system. All these components are explained below.

Static pressure taps

Figure 2.10 shows a schematic of a typical miniature bulged stainless steel tubulation (TUBN063, 1.6mm o.d., 1 mm i.d, Scanivalve Corp.) used for the static pressure

measurements. The pressure taps are connected to the Scanivalve/Swagelok manifolds by flexible vinyl tubes (1.59 mm (0.063") i.d.). One end of the pressure tap is bulged to help secure the vinyl tube to the tap and also ensure a leak proof connection. Also, silicone rubber sealant was applied around the taps at their interface with the stator/outer shroud surface (measurement location) to prevent air leakage.

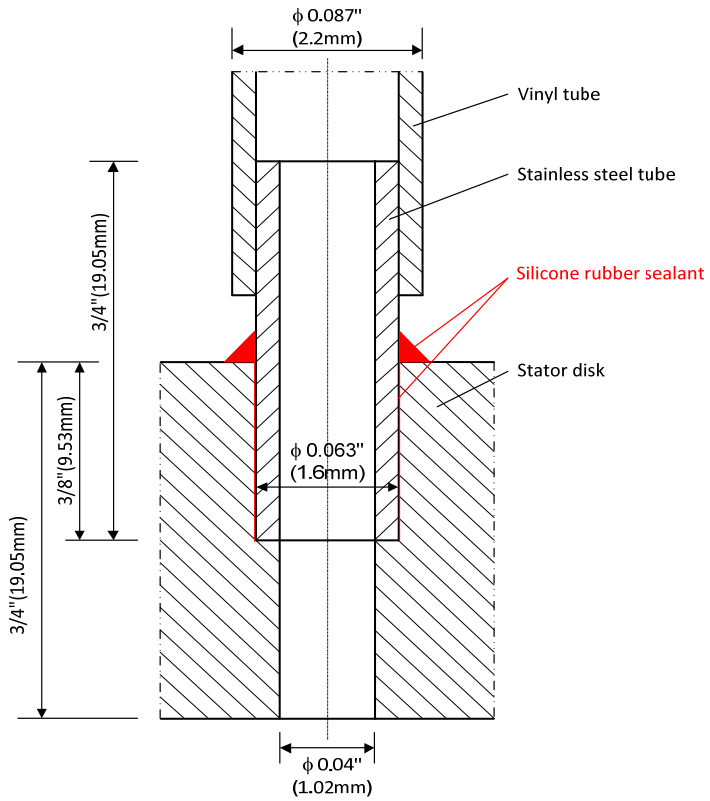

Fig. 2.10 Schematic of a Static Pressure Tap

Measurement locations

Time-averaged static pressures were measured in the main gas path and in the front and aft disk cavities. Pressure taps (as explained earlier) were installed at the locations shown in Figs. 2.5, 2.11, 2.12 and 2.13. For clarity, the following section lists the locations of these pressure taps.

Main gas path

Outer shroud

The static pressures are measured at the main annulus outer shroud as follows:

- at 1.5 mm downstream of the N2 vane trailing edge plane, referred to as 'α' – 10 circumferential locations (of which 9 are over one N2 vane pitch).

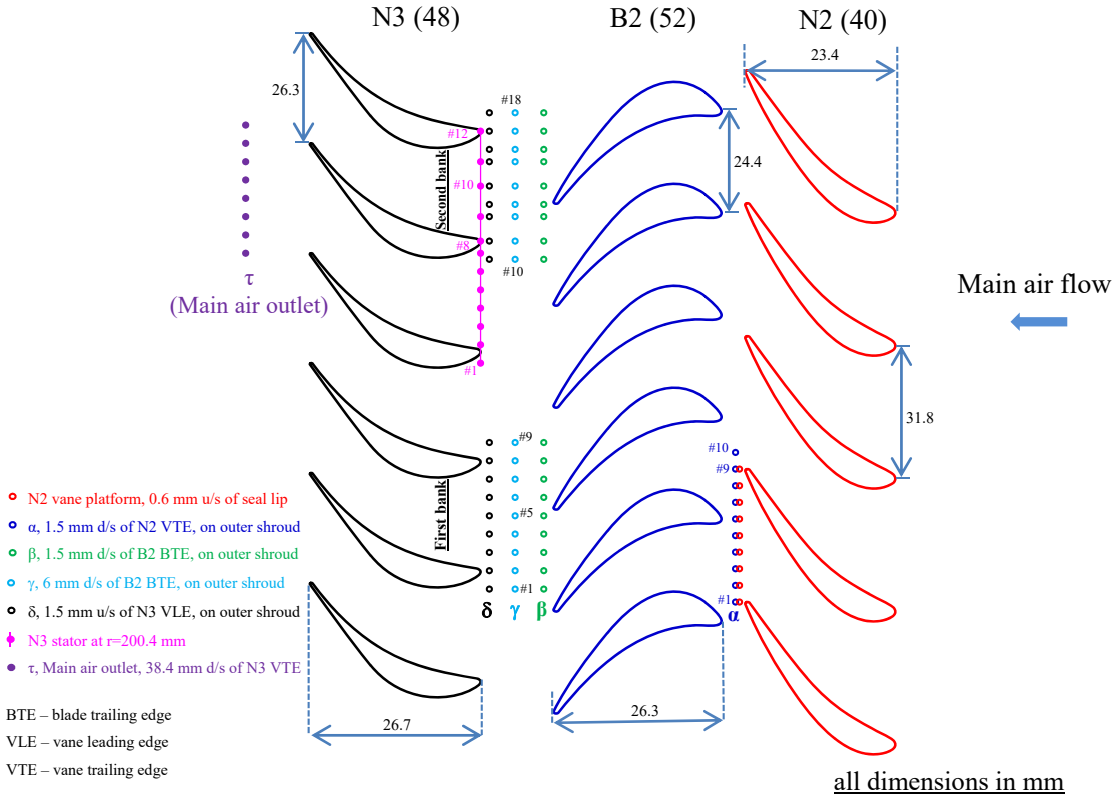

Fig. 2.11 Circumferential Locations of Pressure Taps at the Main Gas Path Outer Shroud, N2 Vane Platform, and Aft Cavity at r =200.4 mm

- at 1.5 mm, 6 mm and 10 mm downstream of the B2 blade trailing edge plane, referred to, respectively, as 'β', 'γ' and 'δ' – 18 circumferential locations at each axial plane. The 18 circumferential locations are comprised of two banks of 9 circumferential locations each (Fig. 2.11). The pressure measured in each port of

the first bank is averaged with the pressure measured at the corresponding port located in the second bank; these pressure ports are at the same angular position with respect to the N3 vane leading edge plane.

N2 Vane platform

- at the platform 0.9 mm downstream of the N2 vane trailing edge plane (0.6 mm upstream of platform lip) – 9 circumferential locations over one N2 vane pitch.

Front disk cavity- on N2 stator surface

- 10 radial locations – 2 in the inner cavity and 8 in the rim cavity – all along an N2 vane trailing edge as shown in Figs. 2.5 and 2.12.
- 9 circumferential locations over one N2 vane pitch at r = 198 mm and r = 194.4 mm – in the rim cavity.
- 16 circumferential locations spaced equally over 360° at r = 116.5 mm in the inner cavity. This is to check the uniformity of purge air flow distribution in the inner cavity. To reduce experiment time, pressure at only 4 circumferential locations (90 degrees apart) were measured.
- 8 circumferential locations spaced equally over 360° at r = 58.4 mm in the inner cavity. This is to check the uniformity of purge air flow distribution in the inner cavity. To reduce experiment time, pressure at only 2 circumferential locations (180 degrees apart) were measured.

Aft disk cavity- on N3 stator surface

- 10 radial locations – 2 in the inner cavity and 8 in the rim cavity – as shown in Figs. 2.5 and 2.13.

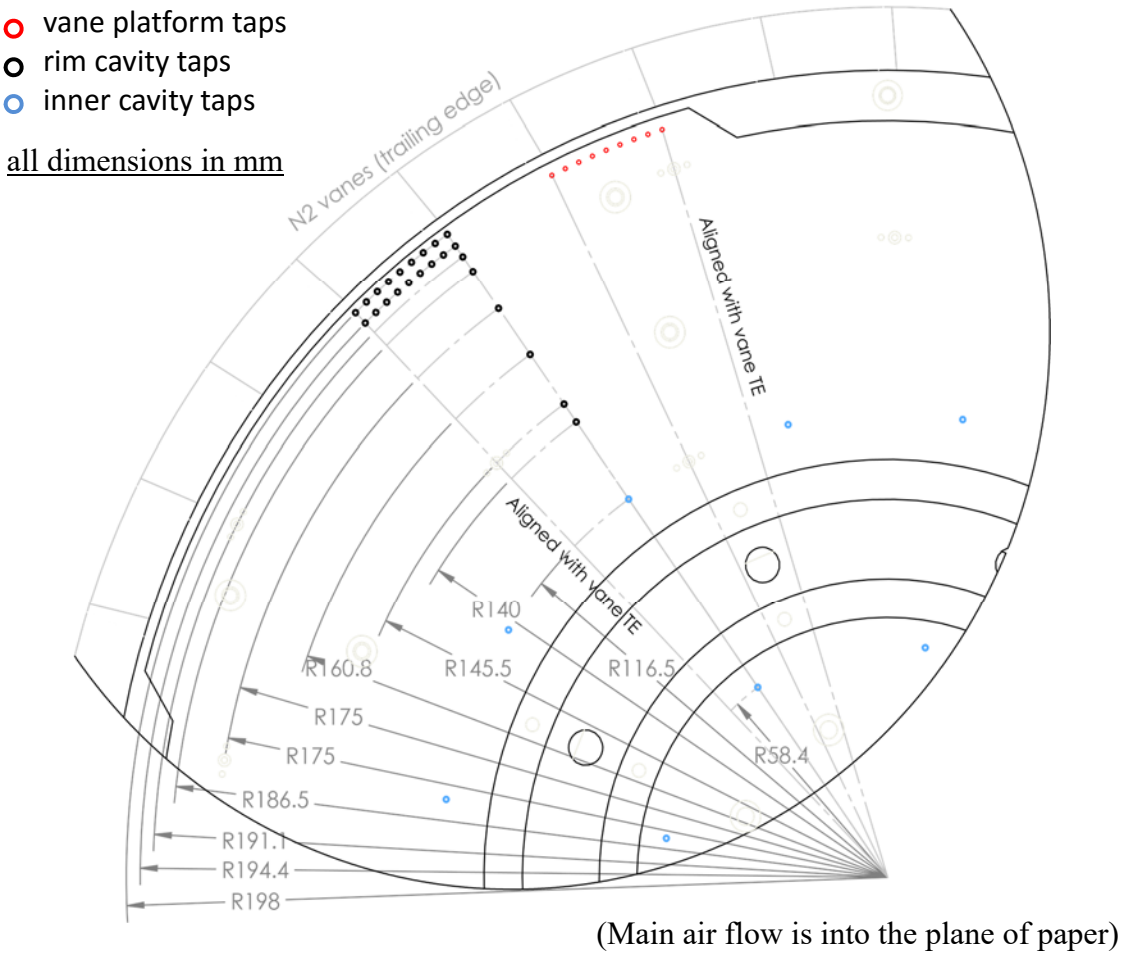

Fig. 2.12 Radial and Circumferential Locations of Pressure and Ingestion Taps on the Front (N2) Stator Surface

- 12 circumferential locations (of which 7 are over one N3 vane pitch) at r = 200.4 mm – in the rim cavity.
- 10 circumferential locations (of which 7 are over one N3 vane pitch) at r = 195.2 mm – in the rim cavity.
- 8 circumferential locations (of which 7 are over one N3 vane pitch) at r = 190.2 mm – in the rim cavity.

- 16 circumferential locations spaced equally over 360° at r = 139.4 mm in the inner cavity. This is to check the uniformity of purge air flow distribution in the inner cavity. To reduce experiment time, pressure at only 4 circumferential locations were measured.
- 2 circumferential locations diametrically opposite each other at r = 65.0 mm in the inner cavity. This is to check the uniformity of purge air flow distribution in the inner cavity.

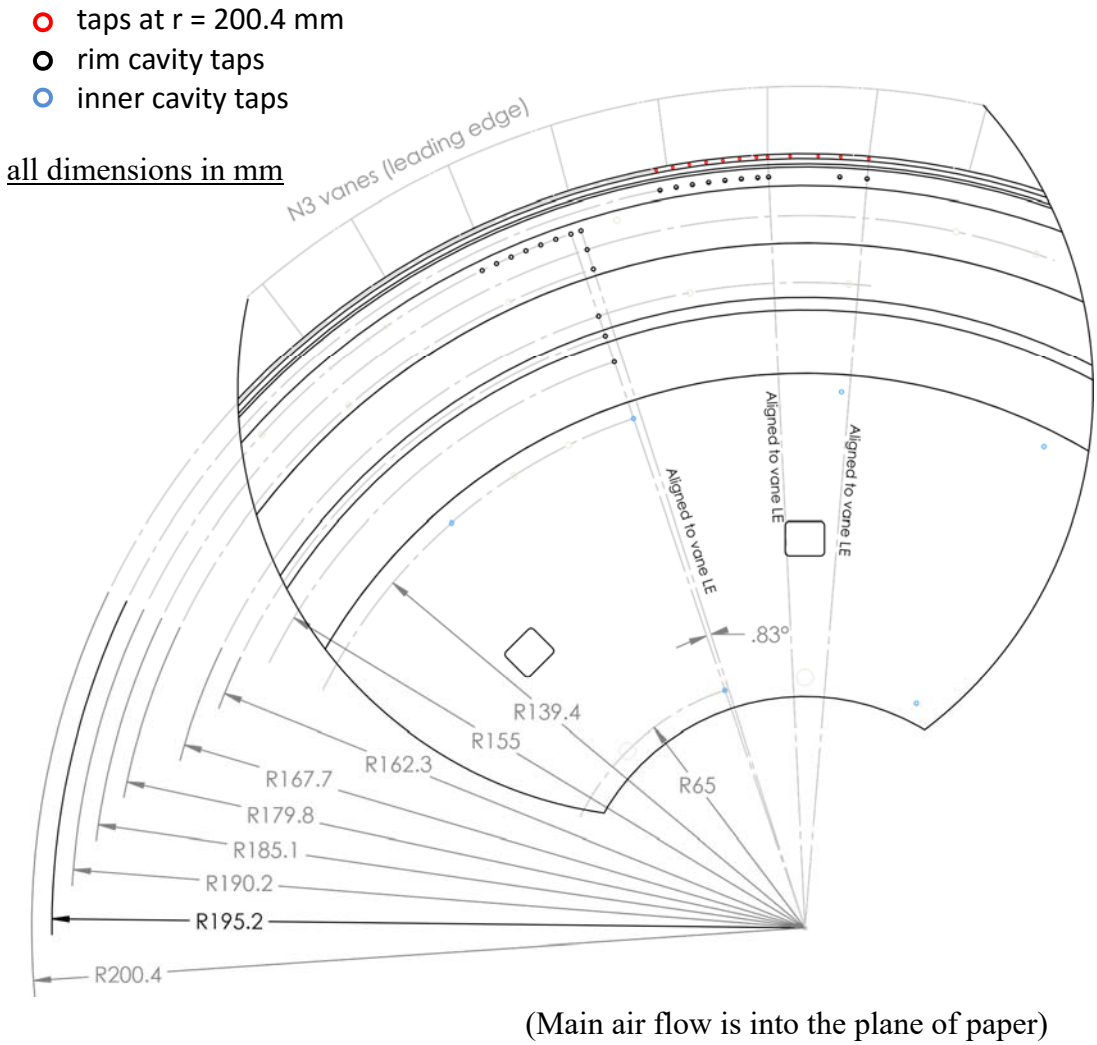

Fig. 2.13 Radial and Circumferential Locations of Pressure and Ingestion Taps on the Aft (N3) Stator Surface

Scanivalve

The Scanivalve is a pressure sampling scanner with 48 inlet channels and one outlet channel. The inlet channels are connected to the pressure taps at the measurement locations via flexible vinyl tubes (1.59 mm (0.063") i.d.) and the outlet channel is connected to the pressure transducer DP45. A solenoid-controlled stepper drive when operated manually, rotates the 48-channel fluid switch wafer such that at any particular time only one of the 48 inlet channels is connected to the output. The inlet channel connected to the outlet channel is identified using a position encoder/decoder which transmits the angular position of the Scanivalve (numbers 0-47) to the display unit.

Swagelok manifold

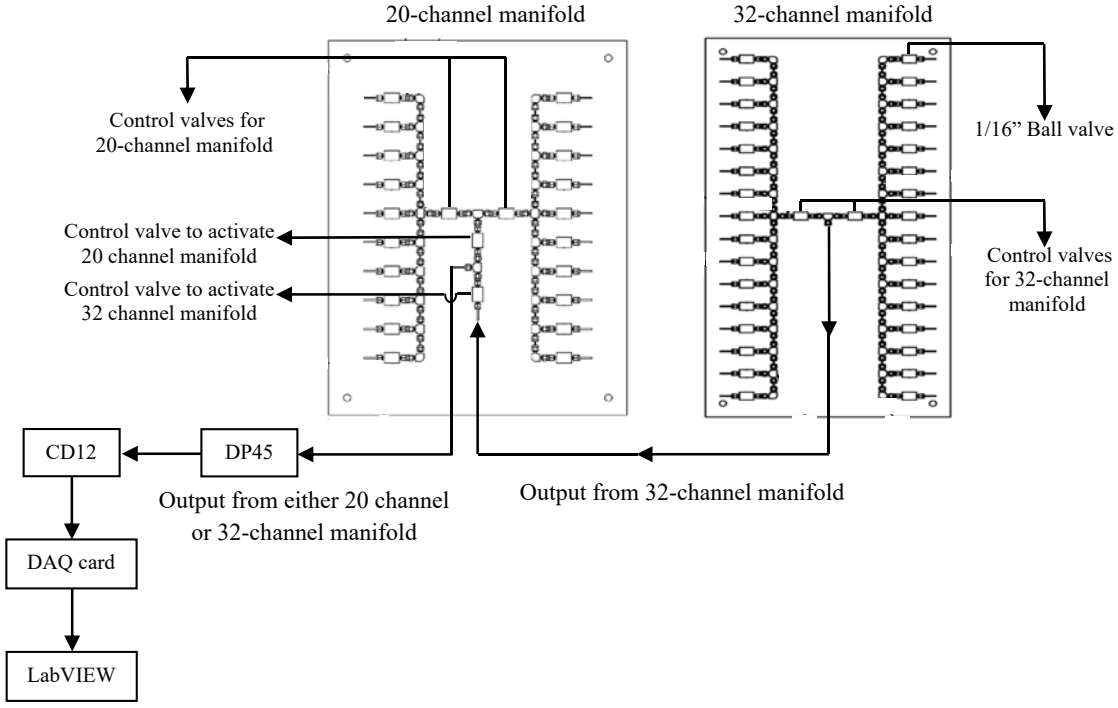

Fig. 2.14 Schematic of the Swagelok Manifolds

Swagelok manifolds with 52 inlet channels and one outlet channel were used in conjunction with the Scanivalve system. The manifolds consist of 52 individual, manually

operated ball valves which connect the desired inlet channel to the outlet channel (Fig. 2.14). The manifolds were built specifically for this work to reduce the number of experimental runs.

Pressure transducer (Validyne DP45)

The static gage pressure was measured by a variable-reluctance type pressure transducer (Validyne DP45) with range of 0 to 13.79 kPa (0 to 2 psi). The transducer has a magnetically permeable diaphragm that is clamped between two stainless steel blocks, each embedded with an inductance coil. The diaphragm is provided with a pressure port on either side, one open to the atmosphere and the other connected to the output of either Scanivalve or one of the Swagelok manifolds. The pressure difference across the diaphragm causes it to deflect towards the low pressure side, thereby changing the inductance in each coil and producing a voltage proportional to the pressure difference sensed.

Pressure signal carrier demodulator (Validyne CD12)

The output voltage from the pressure transducer DP45 is routed to a high-gain pressure signal carrier demodulator (Validyne CD12) which amplifies the signal and also acts as a signal conditioner. Its high input sensitivity range (0.9 to 75 mV/V) allows tracking of even the smallest fluctuations in the input signal. The output is displayed on the front panel and also fed to the data acquisition system.

Data acquisition system

The National Instruments USB 6009 data acquisition card was used to acquire data for the main air flow rate, the static pressure measurement and for the secondary air flow rate. The DAQ card has 16 analog input channels and 16 digital input channels. The analog

voltage signal from digital manometer PS309 (main air flow rate), DP45-CD12 (static pressure), Fluke 45 (purge air flow rate) are input to the DAQ card. The DAQ card is connected to a PC through a USB connection.

LabVIEW 2012 was used to create a program for data acquisition. The data from all the analog inputs of the DAQ card were sampled at 5 kHz for 20 seconds. LabVIEW was programmed such that the time-averaged value of the main air flow rate, static pressure and the secondary flow rate along with their RMS values were displayed on the front panel of LabVIEW. The estimated uncertainty in the static pressure measurements based on instrument and data acquisition system uncertainties is ± 0.5% of the measured static gage pressure.

2.2.2 Experimental Procedure

The required settings for the main blower, secondary blower and the rotor driving system are set on their corresponding controllers. The secondary blower and the motor that drives the rotor are turned on, followed by the main blower. The purge air flow is adjusted using the venturi flow meters and ball valves such that the purge air is split between the front cavity and aft cavity branch by the design ratio of 3:2 respectively. Once the desired main air flow rate, purge air flow rate and rotor rpm are set, the rig is allowed to run for 10 minutes post which measurements are taken.

Boundary temperatures and static pressures

The boundary temperatures and static pressures at the locations shown in Fig. 2.15 are first measured for all experiments.

- Main air inlet pressure and temperature (Fig. 2.5), main air outlet pressure (Fig. 2.5), front and aft cavity purge air inlet pressures and temperatures (Fig. 2.15) constitute the boundary conditions.
- Main air inlet pressure and temperature are measured at 46 mm (1.81”) upstream of the N2 vane leading edge plane at the main annulus outer shroud.
- Main air outlet pressures are measured at 8 circumferential locations over one N3 vane pitch, at an axial distance of 38.4 mm (1.51”) from the N3 stator vane trailing edge.

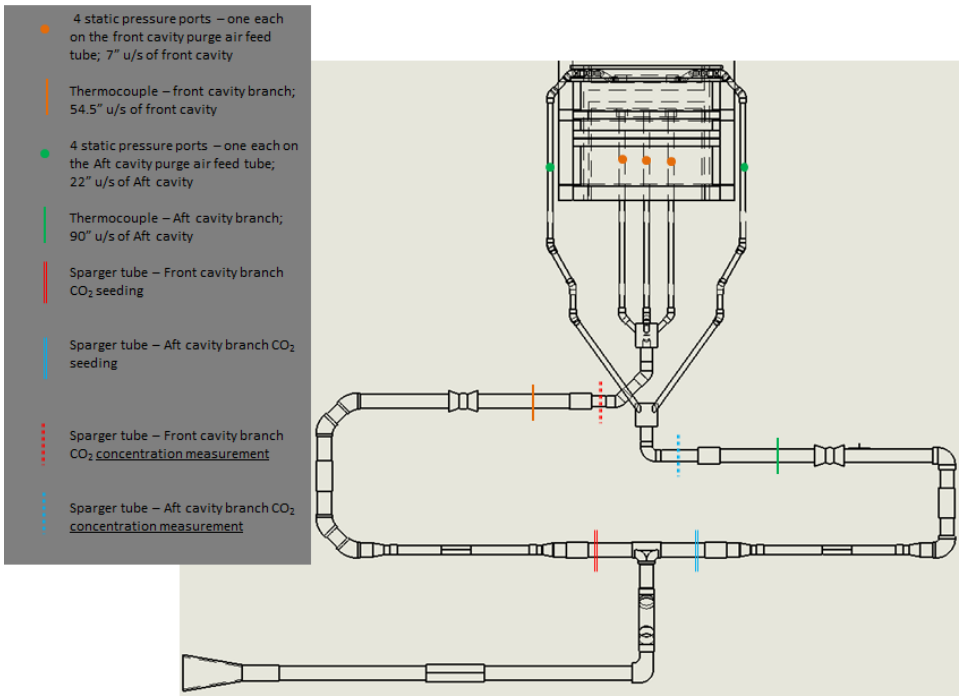

Fig 2.15 Schematic Showing the Locations of CO_2 Seeding and Sampling, Purge Air Inlet Pressure and Temperature Measurements in the Purge Air Flow Network

At a given point of time, either one of the Swagelok manifolds or Scanivalve was connected to DP45. The desired port for measurement is toggled (knobs in Swagelok manifold and stepper control in Scanivalve) and the LabVIEW program is run to sample the data.

2.3 Mainstream Gas Ingestion Measurement

In order to estimate the main gas ingestion into the disk cavity and thereby determine the sealing effectiveness of the rim seal geometry, tracer gas concentration technique was used. The purge air was seeded with a known volumetric concentration of the tracer gas, CO_2. Ingestion of main gas into the disk cavity would result in the reduction of the volumetric concentration of CO_2 in the disk cavity air. Using the measured concentration values of CO_2 in the disk cavity air, purge air supply and main air flow at the inlet, a sealing effectiveness value for the corresponding rim seal is calculated by equation 2.4. An effectiveness value of 0 indicates zero sealing and a value of 1 indicates complete sealing.

$$\eta(\underline{r}) = \frac{C(\underline{r}) - C_{main}}{C_{purge} - C_{main}} \tag{2.4}$$

Tracer gas concentration measurements were carried out at all disk cavity locations (not in the main gas path) where static pressure was measured. The measurements for the front and aft cavities were carried out in separate experimental runs (unlike the pressure measurements in which for a particular purge air flow rate, the front and aft cavity pressures were measured in the same experimental run). This is because, upstream of the aft cavity, the CO_2 supplied to the front cavity mixes with the main air flow. The presence of this additional CO_2 in the main air flow would affect the measured CO_2 concentration values for the aft cavity, if measurements for both the cavities were carried out concurrently. Therefore, depending on the experiment, the tracer gas was injected either in the front cavity branch or in the aft cavity branch (i.e., not in both concurrently).

2.3.1 System Components

NDIR gas analyzer

A NDIR (Non-dispersive Infra-Red) gas analyzer (Siemens-Ultramat 23) was used for measuring the CO_2 concentration in the sample. The rear panel of the analyzer has two inlet ports that are connected to the sample gas and the zero gas (N_2), while the outlet port is open to the atmosphere. The components of the analyzer are an infrared source, safety filter, analyzer chamber, flowmeter and pump. An external oval-diaphragm pump (Thomas 40026009) was employed along with the analyzer's pump to provide the required sample gas flow rate. The permissible ranges for the sample gas flow rate, pressure and temperature were 1.1 to 2 l/min, 0.5 to 1.5 bar and 0 to 50°C respectively. The flow meter on the front panel of the analyzer shows the sample gas flow level.

When turned on, the analyzer performs an auto-calibration (AUTOCAL) with the supplied zero gas (ultra-high purity N_2). This AUTOCAL adjusts the zero point and sensitivity of the IR channel. This was done automatically once every three hours to compensate for variation in the ambient conditions.

The working of the analyzer is based on the principle of molecule-specific absorption of bands of infrared radiation. The infrared radiation from the source passes on to the analyzer chamber into which the sampled gas is flowing. The IR radiation is weakened as a function of the concentration of CO_2. An electric signal is generated proportional to the CO_2 concentration and the concentration value of CO_2 is displayed on the analyzer's front panel.

Gas cylinders and tube connections

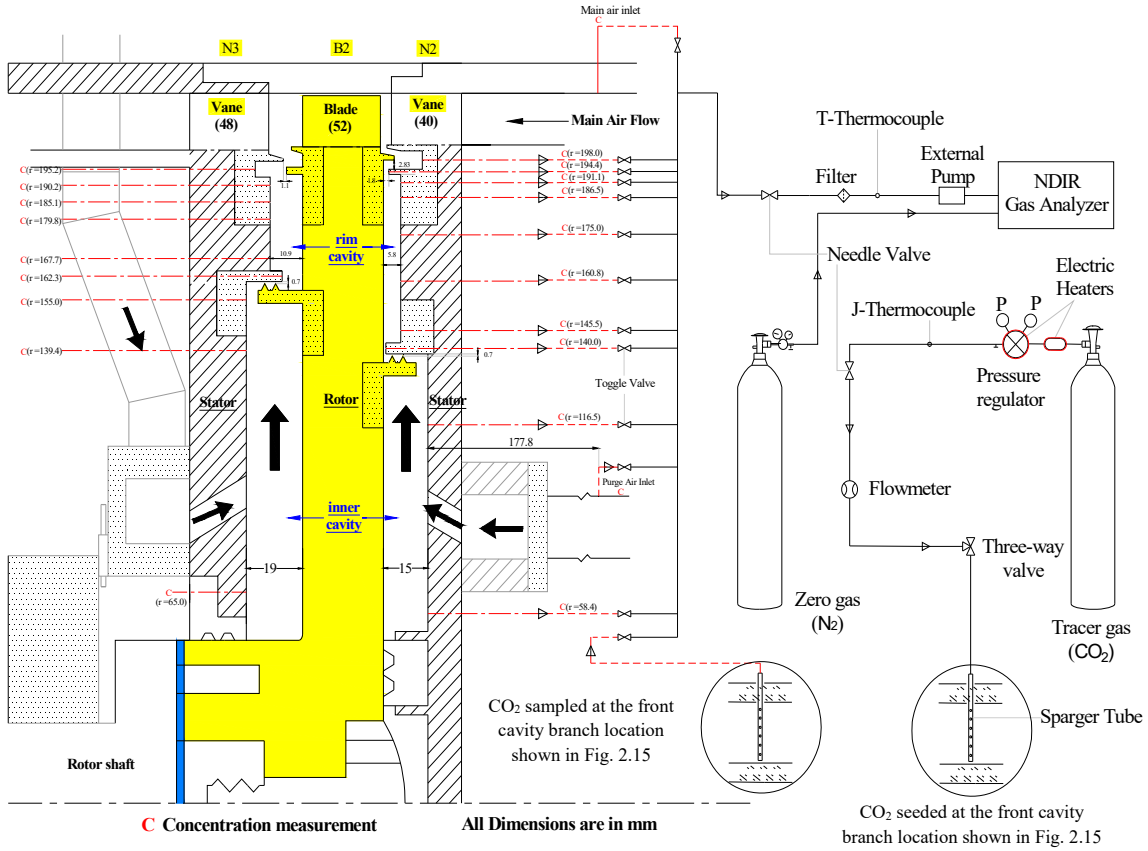

Fig. 2.16 Schematic of the Mainstream Gas Ingestion Measurement System

Sparger tubes with 15 holes; each hole being 1 mm in diameter are used to seed and sample CO_2 in the purge air flow network at the locations shown in Fig. 2.15. The CO_2 flow rate is controlled using a pressure regulator and needle valve (shown in Fig. 2.16) such that the desired concentration of 4.0 % by volume of CO_2 is obtained at the purge air inlet to the cavity. To regulate the temperature of the gas to be within ±1°C of the purge air, an electric gas heater in between the cylinder and pressure regulator and a band heater at the back of the regulator are used.

The concentration measurement taps (same static pressure taps) are connected to individual toggle valves by means of vinyl tubes (3/16” ID , 5/16” OD). The valves are

connected together in the form of a manifold with a common outlet. A needle valve and a filter are downstream of this outlet. The exit of the filter is connected to an external pump, which is then connected to the sampling port of the analyzer using vinyl tubes.

The concentration measurements are time-averaged over many rotor revolutions since each measurement takes some time. However, the concentrations measured are local with respect to the vane position as well as the radial position on the stator surface. The flow of sample gas through the analyzer chamber of the gas analyzer is Steady State Steady Flow (SSSF). The sample gas is supplied at a constant flow rate of 1.5 l/min; the analyzer chamber pressure depends on the ambient pressure and remains constant even when the pressure at the sampling location changes. The uncertainty in the concentration measurement is ±0.11% CO_2 concentration (this translates to ±0.17% mass concentration).

2.3.2 Experimental Procedure

The gas analyzer is started and the zero gas (N_2) is supplied for auto-calibration. As discussed in the static pressure measurement section, the test rig is allowed to run for 10 minutes. The boundary pressures and temperatures are measured. CO_2 is then supplied to the desired purge air branch. The desired CO_2 flow rate is set using the pressure regulator and needle valve by monitoring the concentration of CO_2 (4.0 % by volume) in the purge air branch before its entry into the cavity.

Once the desired CO_2 concentration in the purge air branch is set, the CO_2 concentration in the purge air feed tubes are checked for uniform distribution. The CO_2 concentration at the various locations are then measured by toggling their corresponding toggle valves. The CO_2 concentration value in the purge air supply is monitored after each disk cavity location measurement.

CHAPTER 3

RESULTS AND DISCUSSION

3.1 Experimental Conditions

Experiments were carried out for three experiment sets to study main gas ingestion into the front and aft disk cavities. Each experimental set is defined by the following non-dimensional parameters: main air flow Reynolds number (Re_{R_h}), rotational Reynolds number (Re_ϕ) and purge air mass flow rate c_w (Table 3.1).

Table 3.1 Experimental Conditions

			Purge air flow rate distribution								
Expt. Set	**Rotor speed**	**Main air flow rate**	**Front Cavity [60%]**			**Aft Cavity [40%]**			**β_2 [°]**	**α_3 [°]**	**V_{a2}/U**
	rpm/Re_ϕ	cfm/Re_{Rh}	cfm	$c_{w,f}$	% main air flow	cfm	$c_{w,a}$	% main air flow			
I	2650/ 7.35×10^5	1325/ 3.90×10^5	0	0	0	0	0	0	37.1	-14.9	0.51
			6	909	0.453	4	606	0.302			
			12	1818	0.906	8	1212	0.604			
			18	2726	1.358	12	1818	0.906			
			24	3635	1.811	16	2423	1.208			
II	2950/ 8.18×10^5	1475/ 4.34×10^5	0	0	0	0	0	0	37.1	-14.9	0.51
			6	909	0.407	4	606	0.271			
			12	1818	0.814	8	1212	0.542			
			18	2726	1.220	12	1818	0.814			
			24	3635	1.627	16	2423	1.085			
III	3250/ 9.01×10^5	1625/ 4.78×10^5	0	0	0	0	0	0	37.1	-14.9	0.51
			6	909	0.369	4	606	0.246			
			12	1818	0.738	8	1212	0.492			
			18	2726	1.108	12	1818	0.738			
			24	3635	1.477	16	2423	0.985			

The main air flow rate and the rotor speed were chosen such that the value of β_2 was maintained at a large positive value to ensure that the rotor operated as a turbine. For all the experiment sets, this value was kept constant, since velocity triangles influence the ingestion process [40] . The value of rotational Reynolds number Re_ϕ is an order of magnitude lower than the actual gas turbine operating conditions. The estimated uncertainties in the values of the non-dimensional quantities Re_ϕ, Re_{R_h} and c_w are respectively ± 0.5%, ± 1% and ± 1.5%.

Time-averaged static pressure measurements and tracer gas concentration measurements were carried out for the experiment conditions shown in Table 3.1. The mass flow rate of ingested air from the main annulus into the rim cavities ($c_{w,ing,f}$ and $c_{w,ing,a}$) for the various experiment sets are reported. All the experiments were carried out in laboratory conditions with the ambient air at an average temperature of 23°C and pressure of 102000 Pa. For brevity, the results of Expt. sets I and III are discussed here for the highest purge air flow condition ($c_{w,f}$ = 3635 and $c_{w,a}$ = 2423).

3.2 Front Disk Cavity Results

3.2.1 Time-averaged Static Pressure Distribution

The time-averaged static pressure was measured in the main gas path (α-plane and N2 vane platform) and at all the front disk cavity locations as explained in Section 2.2. The N2 stator vanes turn the main air flow at an angle of 69.8°. Circumferential pressure asymmetry is created in the main air flow due to the blockage of flow by the vanes. The magnitude of the peak-to-trough pressure difference of this circumferential pressure, plays an important role in driving ingestion into the disk cavity [32].

Figures 3.1 and 3.2 show the circumferential distribution of time-averaged static gage pressure at the outer shroud (α-plane), N2 stator vane platform (0.9 mm d/s of N2 vane trailing edge) and front rim cavity radial locations r =198.0 mm and r =194.4 mm for Expt. sets I and III at $c_{w,f}$ = 3635, respectively. For both the Expt. sets, the circumferential average static pressure level at the outer shroud is higher than that at the N2 vane platform. This is due to the swirl in the annulus imparted by the vanes, causing a radial pressure gradient. Also, the peak-to-trough pressure asymmetry amplitude is lower at the N2 vane platform than at the outer shroud. The peak-to-trough pressure asymmetry amplitude at the

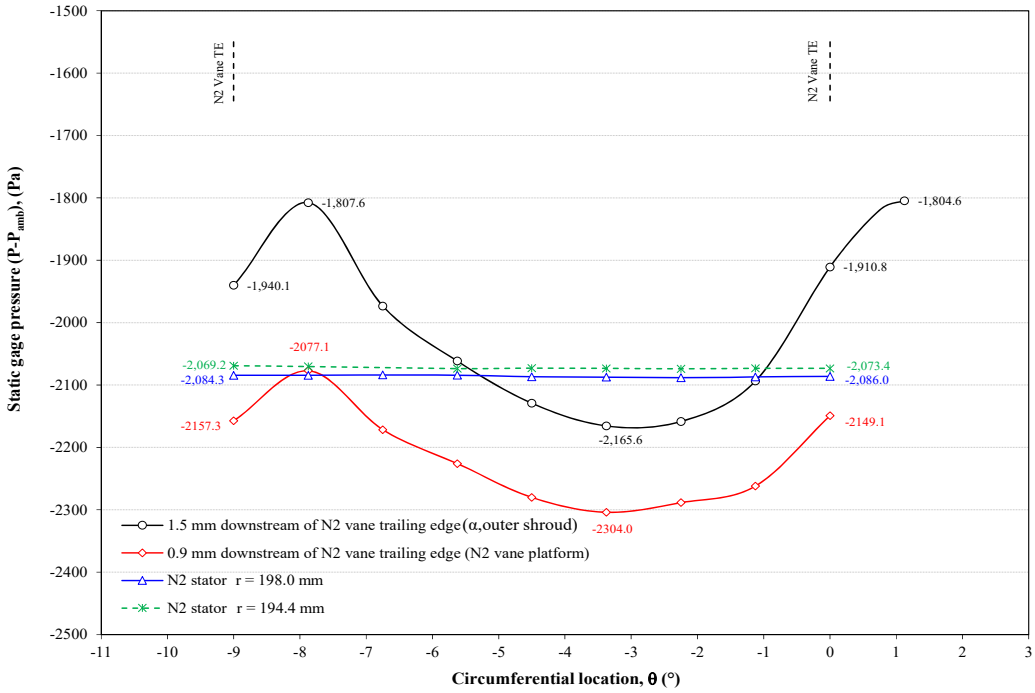

Fig. 3.1 Circumferential Distributions of Static Gage Pressure at the Main Gas Annulus Outer Shroud α plane, N2 Vane Platform, and N2 Stator Surface at Two Radial Locations in the Rim Cavity – Expt. Set I, $c_{w,f}$ =3635

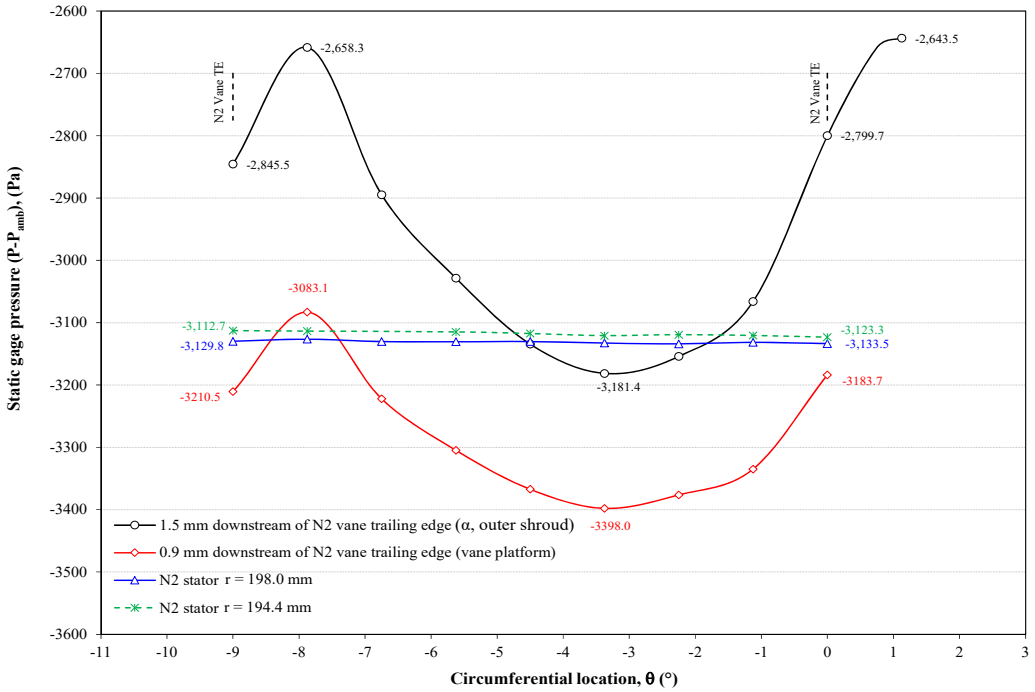

Fig. 3.2 Circumferential Distributions of Static Gage Pressure at the Main Gas Annulus Outer Shroud α plane, N2 Vane Platform, and N2 Stator Surface at Two Radial Locations in the Rim Cavity – Expt. Set III, $c_{w,f}$ =3635

outer shroud and N2 vane platform increases as the main air flow rate increases. There is no discernible circumferential pressure asymmetry at the radial locations r =198.0 mm and r =194.4 mm indicating dissipation of the main air flow asymmetry across the rim seal. The static pressure difference between representative locations in the main gas path and disk cavity is assumed to drive main gas ingestion [22]. For the front disk cavity, the difference between the static pressure measured at the N2 vane platform, 0.9 mm downstream of the N2 vane trailing edge (main gas path) and the rim cavity radial location r = 194.4 mm (disk cavity) is assumed to drive ingestion. The above trends hold good for Expt. set II as well; the circumferential pressure asymmetry amplitude at the α-plane and N2 Vane platform is lesser than Expt. set III and greater than Expt. set I.

Figures 3.3 and 3.4 show the influence of purge air flow rate on the static pressure distribution at the locations discussed above. It is observed that for both the Expt. sets, the N2 vane platform shows noticeable increase in the static pressure level, with the purge air flow rate. There is substantial increase in the static pressure level with purge air flow rate at the radial locations r = 198.0 mm and r = 194.4 mm. Also, the static pressure level at the radial location r = 198.0 mm is greater than at r = 194.4 mm for the lower purge air flow rates, and it is about the same at $c_{w,f}$ =1818. At $c_{w,f}$=2726 and $c_{w,f}$=3635, the static pressure level at r = 194.4 mm is greater than that at r = 198.0 mm which could be due to the increased purge-air-flow restriction posed by the inner seal of the double rim seal; thereby pressurizing the cavity further. There is no significant change in static pressure level observed at the α-plane for Expt. set I, while there is a slight increase for Expt. set III with increase in purge air flow rate. The peak-to-trough amplitude at the α-plane and the vane platform decreases with the increase in purge air flow rate, possibly due to the interaction

of rim cavity egress flow with the main air flow. Thus increasing $c_{w,f}$ decreases the peak-to-trough pressure asymmetry amplitude at the N2 vane platform and increases the static pressure at the rim cavity radial location r = 194.4 mm, thereby reducing the potential for main gas ingestion into the front disk cavity. The above described trends remain the same for Expt. set II.

Figures 3.5 and 3.6 show for Expt. sets I and III respectively, the radial distributions of time-averaged static gage pressure in the front disk cavity at N2 stator surface for the various purge air flow rates. It is observed that, for both the Expt. sets, the static pressure level in the inner cavity increases substantially with purge air flow rate due to the presence of labyrinth seal restricting the flow, thereby pressurizing the inner cavity. The pressure drop across the labyrinth seal increases with the purge air flow rate. This qualitatively points out that the ingested air will progressively tend to be confined within the rim cavity, proving the labyrinth seal to be very effective in protecting the inner cavity. The rim cavity also shows the trend of increasing static pressure level with purge air flow rate but the corresponding increase in static pressure level is lower than the inner cavity. The radial pressure gradient observed in the rim cavity could be primarily due to the tangential motion (rotation) of the cavity fluid. The negative gradient in static pressure between the radial locations r = 191.1 mm and r = 194.4 mm increases with the purge air flow rate, suggesting that the transportation of the ingested air radially inboard of r = 194.4 mm becomes progressively difficult. Hence most of the ingested air will be confined within the wheelspace of the double rim seal and exhausted back to the main gas path. The trend remains the same for Expt. set II.

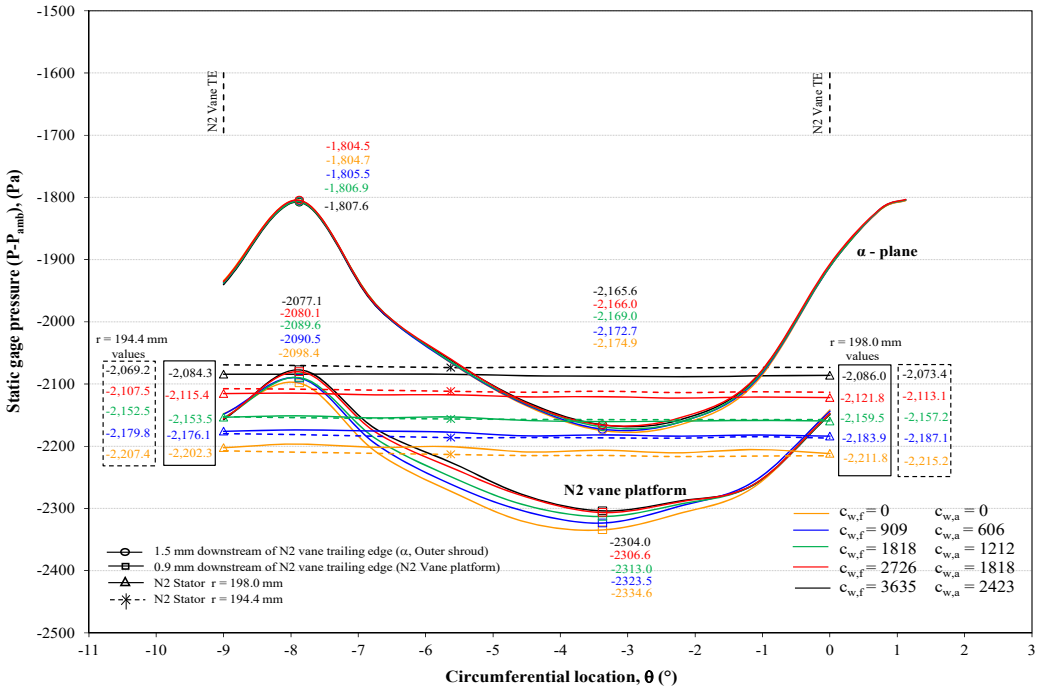

Fig. 3.3 Circumferential Distributions of Static Gage Pressure at the Main Gas Annulus Outer Shroud α plane, N2 Vane Platform, and N2 Stator Surface at Two Radial Locations in the Rim Cavity – Expt. Set I Conditions

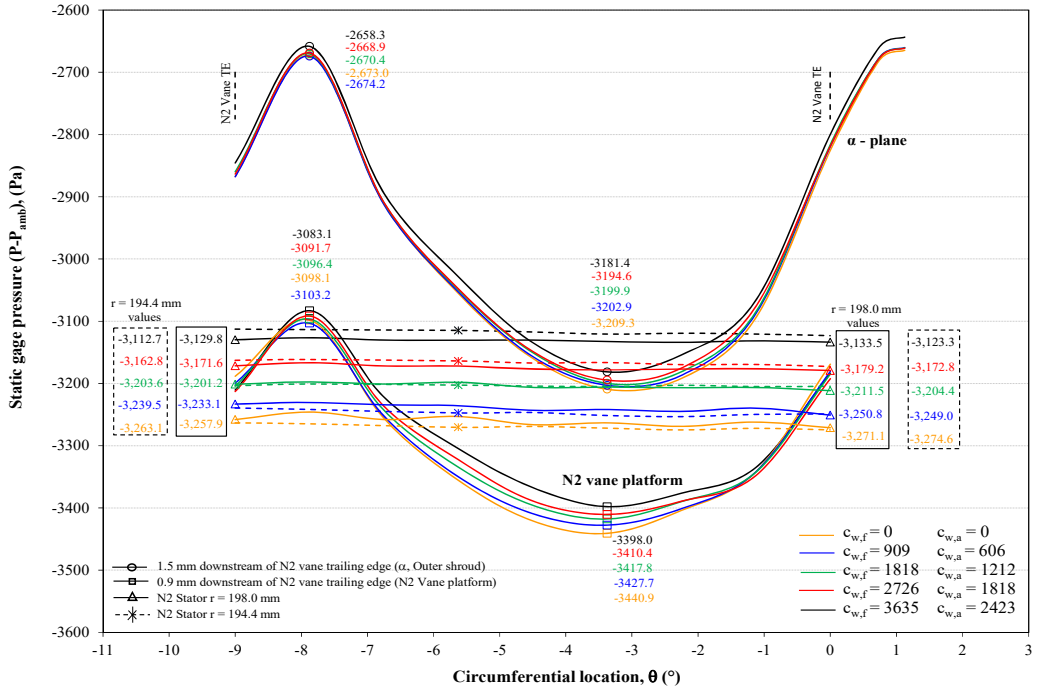

Fig. 3.4 Circumferential Distributions of Static Gage Pressure at the Main Gas Annulus Outer Shroud α plane, N2 Vane Platform, and N2 Stator Surface at Two Radial Locations in the Rim Cavity – Expt. Set III Conditions

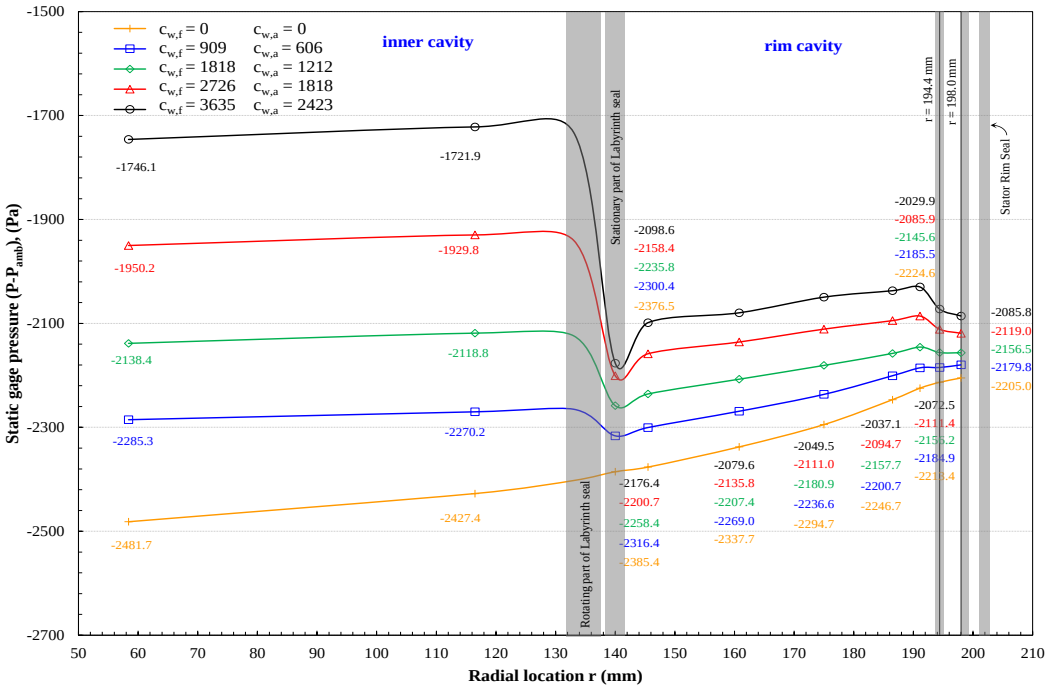

Fig. 3.5 Radial Distributions of Static Gage Pressure in the Front Disk Cavity at N2 Stator Surface – Expt. Set I conditions

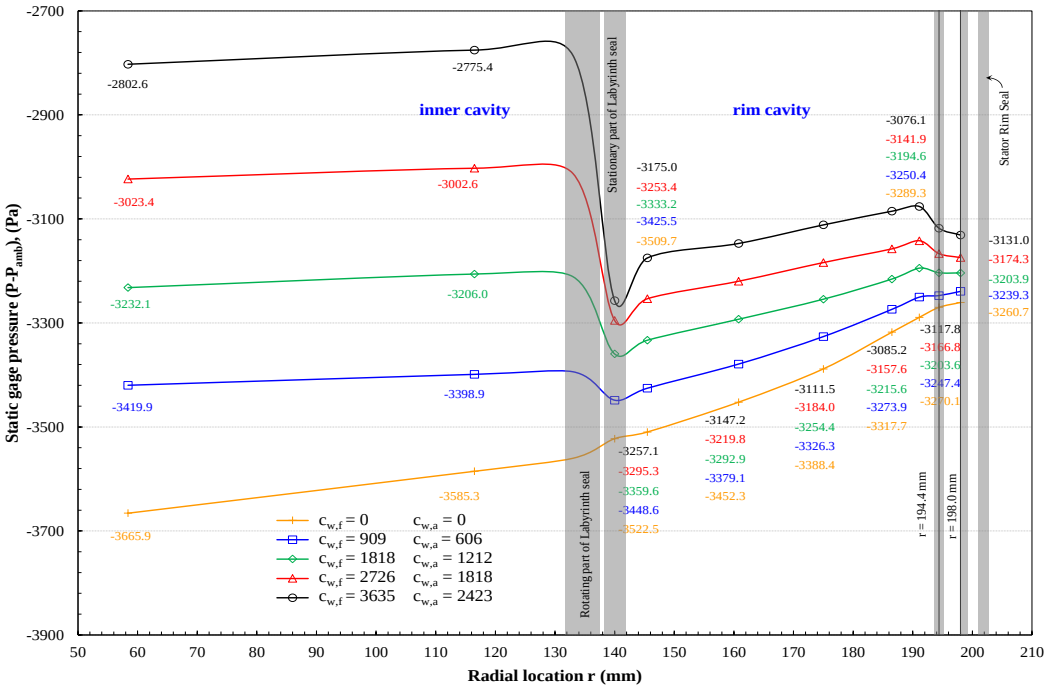

Fig. 3.6 Radial Distributions of Static Gage Pressure in the Front Disk Cavity at N2 Stator Surface – Expt. Set III conditions

3.2.2 Mainstream Gas Ingestion Distribution

Tracer gas (CO_2) concentration measurements were carried out at all the front disk cavity locations where static pressure was measured. The sealing effectiveness is defined by Eq. 2.4.

CO_2 concentration was measured in the front inner cavity at the radial locations r = 116.5 mm (four circumferential locations 90° apart) and r =58.4 mm (two circumferential locations 180°apart) for all three Expt. sets. It was observed that the mixing of CO_2 with the purge air in the supply pipe was complete, prior to the inner cavity entry at the high purge air flow rates ($c_{w,f}$ = 3635, 2726), but becomes progressively incomplete at the two low purge air flow rates ($c_{w,f}$ = 1818, 909). It is reasoned that the 90° turn of the purge air flow after entering the inner cavity led to complete mixing at the low purge flows. As such, the circumferentially-averaged CO_2 concentration at the radial location r =116.5 mm is adopted as the CO_2 concentration in the purge air supplied (C_{purge}). This value was used in the calculation of sealing effectiveness for the entire front disk cavity (rim as well as inner).

Figures 3.7 and 3.8 show the radial distributions of local sealing effectiveness for Expt. sets I and III respectively, in the front disk cavity at the N2 stator surface for the four purge air flow rates. For both the Expt. sets, the sealing is near-perfect in the inner cavity at all the four purge air flow rate. Both the sets follow a similar trend of sealing effectiveness distribution in the rim cavity; the effectiveness level increases substantially as the purge air flow rate is increased from $c_{w,f}$ = 909 to $c_{w,f}$ = 1818. The increase in effectiveness level decreased for the higher purge air flow rates. The effectiveness level for Expt. set I at all the purge air flow rates is higher than the effectiveness level for Expt. set III. The reason being that the higher main air flow rate and higher rotor rotational speed

for Expt. set III leads to greater peak-to-trough pressure asymmetry and disk pumping, favoring more ingestion. There is a substantial drop in the sealing effectiveness level across the rim seal which shows the good sealing performance of the rim seal. The gradient of sealing effectiveness between radial locations r = 191.1 mm and r = 194.4 mm, becoming more negative with the increase in purge air flow rate suggests, progressive difficulty for the transportation of ingested air radially inboard of r = 194.4 mm. This was also inferred from the static pressure measurements. Hence most of the ingested air tends to be confined within the wheelspace of the double rim seal. Moreover, the circumferential pressure asymmetry attenuates at the radial locations r = 198.0 mm and r = 194.4 mm, suggesting that EI ingestion would dominate in the wheelspace radially outboard of the inner seal of the double rim seal, and RI ingestion would dominate in the disk cavity, radially inboard of the inner seal of the double rim seal [35]. Similar trend was observed for Expt. set II, but the effectiveness level at all four purge air flow rates was greater than Expt. set III and lesser than Expt. set I.

Figure 3.9 shows the variation of sealing effectiveness (η) with purge air flow rate on N2 stator surface at r = 191.1 mm for all three Expt. sets. A best fit curve is drawn for each Expt. set, connecting the corresponding data points. It is observed that Expt. set I has higher sealing effectiveness than the other two Expt. sets at this radial location for all the purge air flow rates. The increase in sealing effectiveness for the lower purge air flow rates is sharp, but tends to increase only by small amounts at higher purge air flow rates, for all three Expt. sets. It is to be noted that, all the curves seem to converge at the higher purge air flow rates. Similar trend was observed at the radial location r = 194.4 mm.

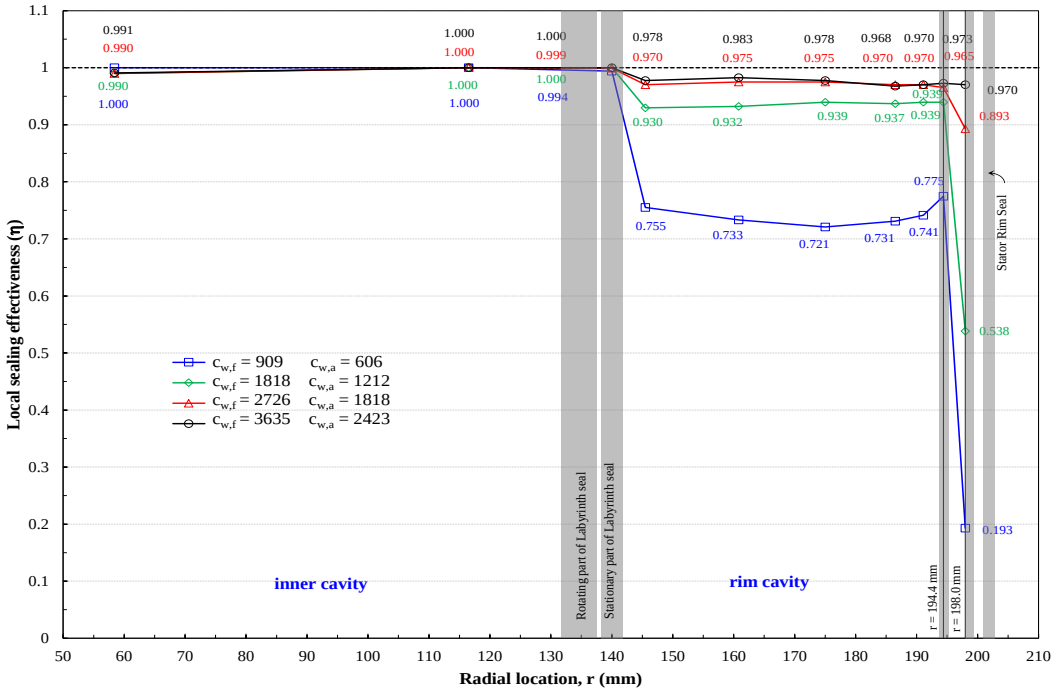

Fig. 3.7 Radial Distributions of Sealing Effectiveness in the Front Cavity at N2 Stator Surface - Expt. Set I conditions

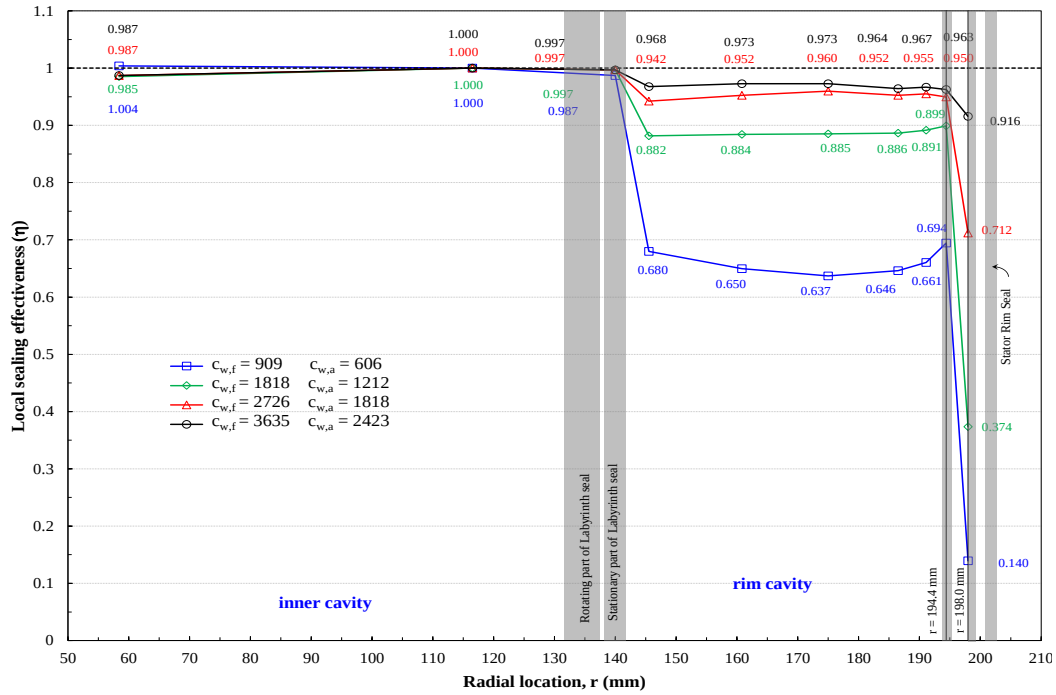

Fig. 3.8 Radial Distributions of Sealing Effectiveness in the Front Cavity at N2 Stator Surface - Expt. Set III conditions

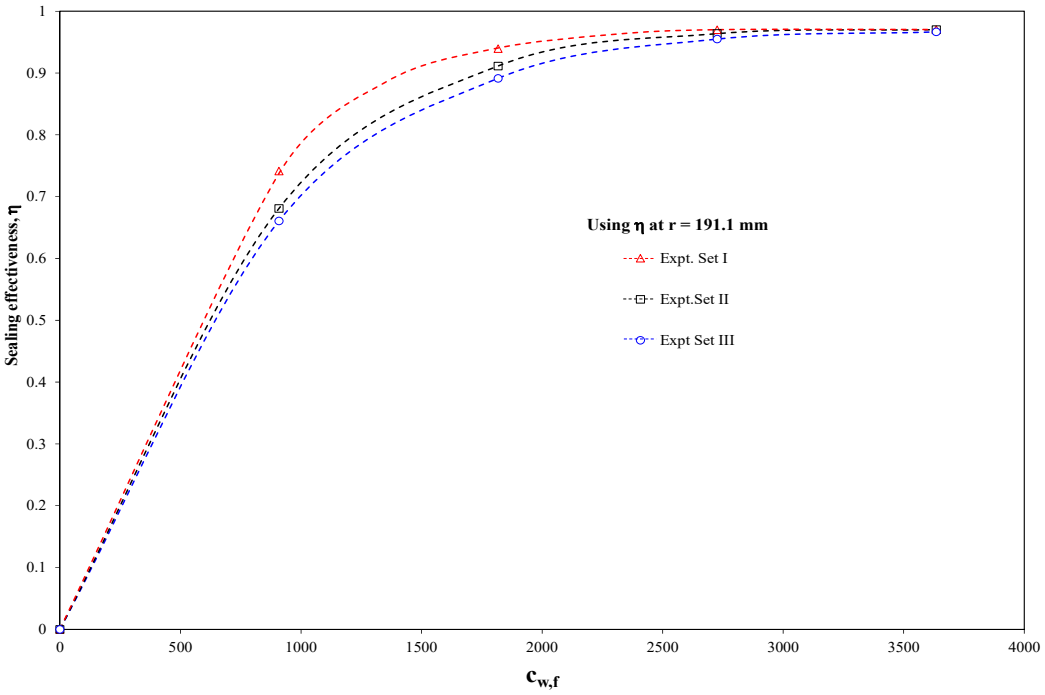

Fig. 3.9 Variation of Sealing Effectiveness with $c_{w,f}$ in the Front Rim Cavity at r =191.1mm on N2 Stator Surface for the Three Expt. Sets

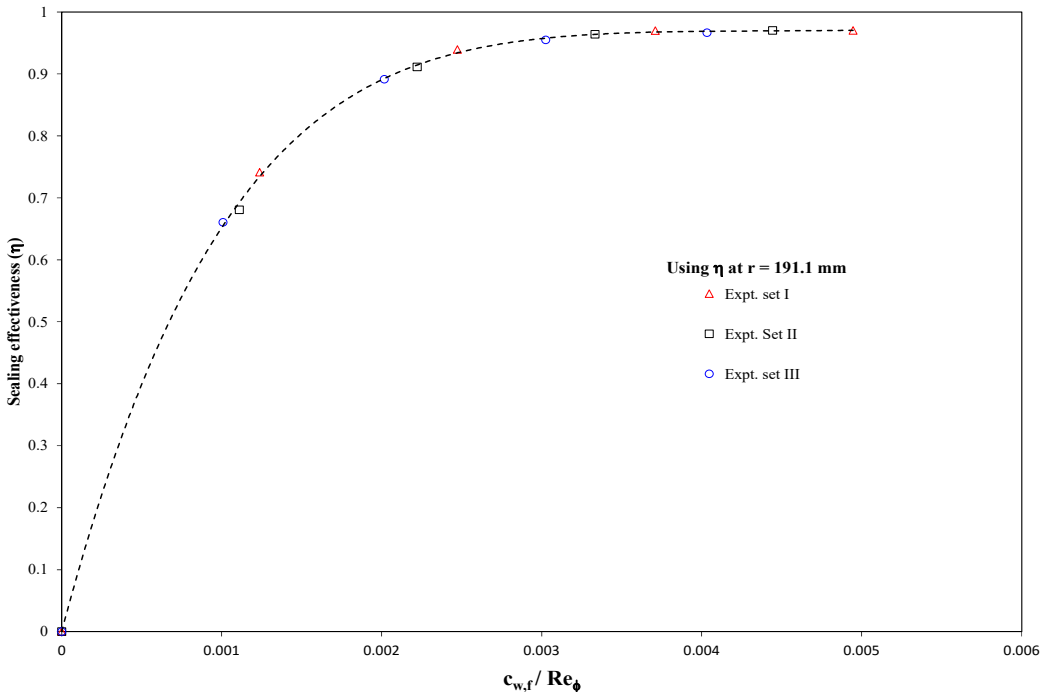

Fig. 3.10 Variation of Sealing Effectiveness with $c_{w,f}/Re_\phi$ in the Front Rim Cavity at r =191.1 mm on N2 Stator Surface for the Three Expt. Sets

Figure 3.10 shows the distribution of sealing effectiveness with $c_{w,f}/Re_{\phi}$ (this is equal to $[V_{rim\ seal,f}/U].2\pi G_{c,f}$) for all three Expt. sets at r = 191.1 mm. The sealing effectiveness of all the Expt. sets collapse onto a single curve. Similar trend is observed at r = 194.4 mm.

The non-dimensional mass flow rate of air, ingested from the main annulus into the front rim cavity ($c_{w,ing,f}$) can be found using the equation,

$$c_{w,ing,f} = \left(\frac{1}{\eta} - 1\right) c_{w,f} \tag{3.1}$$

Figure 3.11 shows the variation of $c_{w,ing,f}$ with $c_{w,f}$ for the front cavity at N2 stator surface radial locations r = 198.0 mm, r = 194.4 mm and r = 191.1 mm for the three Expt. sets. Also, shown are the best-fit curves for the data points. It is observed that $c_{w,ing,f}$ decreases with increase in $c_{w,f}$. Also, $c_{w,ing,f}$ at the radial location r = 198.0 mm for all the Expt. sets is substantially greater than that at the other two radial locations. This suggests that a substantial amount of the ingested air flows back to the main annulus, while a small amount gets ingested radially inboard past the seal at r = 194.4 mm. It is to be noted that all the curves tend to converge as the purge air flow rate increases. $c_{w,ing,f}$ for Expt. set III is higher than Expt. sets I and II for all the values of $c_{w,f,}$ due to the higher main air flow rate and rotational speed, favoring more ingestion.

Figure 3.12 shows the variation of $c_{w,ing,f}/c_{w,f}$ with $c_{w,f}/Re_{\phi}$ for the front rim cavity at the N2 stator surface radial locations r = 194.4 mm and 191.1 mm for the three experiment sets. Best- fit curves drawn for each radial location converge onto a single curve at higher values of $c_{w,f}/Re_{\phi}$. Also, the extrapolated curve tends to be asymptotic in nature which suggests that a performance limit exists for the front rim seal, where increasing the

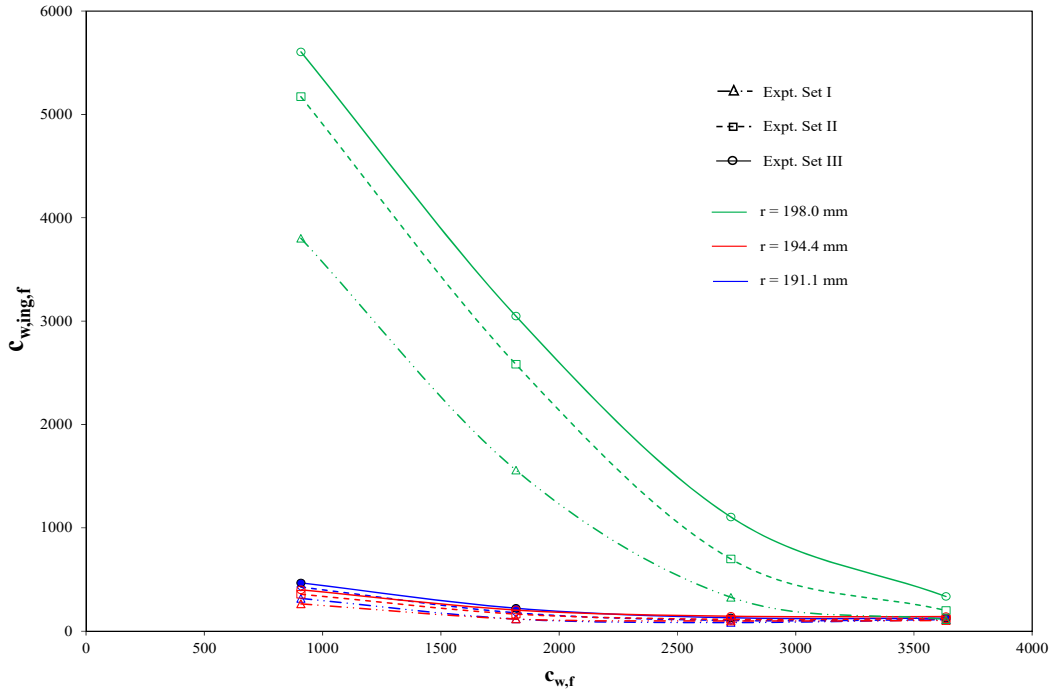

Fig. 3.11 Variation of $c_{w,ing,f}$ with $c_{w,f}$ in the Front Rim Cavity at N2 Stator Surface r = 191.1 mm, 194.4 mm, and 198.0 mm for the Three Expt. Sets

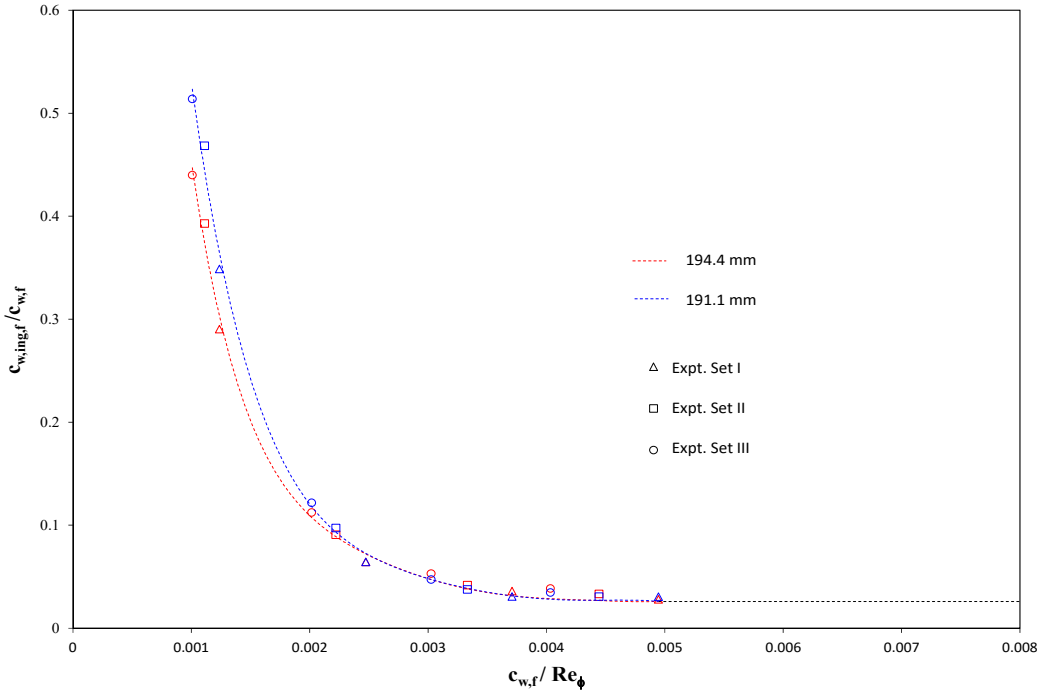

Fig. 3.12 Variation of $c_{w,ing,f}/c_{w,f}$ with $c_{w,f}/Re_{\phi}$ in the Front Rim Cavity at N2 Stator Surface r = 191.1 mm and 194.4 mm for the Three Expt. sets

purge air flow rate beyond a value would not help in reducing ingestion any further, and that the front rim cavity would never be completely sealed. This is also evident from the asymptotic trend observed in Figs. 3.9 and 3.10. The effectiveness values used for the above calculations at the radial locations r =198.0 mm and 194.4 mm were those obtained at their corresponding circumferential location aligned with a N2 vane trailing edge.

3.3 Aft Disk Cavity Results

3.3.1 Time-averaged Static Pressure Distribution

The time-averaged static pressure was measured in the main gas path (β, γ, and δ planes) and at all the aft disk cavity locations as discussed in Section 2.2.

Figures 3.13 and 3.14 show the circumferential distributions of time-averaged static gage pressure at the main annulus outer shroud (β, γ, δ planes) for Expt. Sets I and III at $c_{w,a}$ =2423 respectively. For each axial location, the static pressure measured at a particular circumferential location of the first bank is averaged with the static pressure measured in the corresponding circumferential location in the second bank. The plots shown are the averaged values. Comparing Figs. 3.13 and 3.14 we observe that the peak-to-trough pressure asymmetry amplitude at all the outer shroud measurement planes, increase with the main air flow rate. Also, the peak-to-trough pressure asymmetry increases with the increase in axial distance from B2 blade trailing edge plane. This is because of the blockage of the main air flow by the N3 stator vanes. The increase in peak-to-trough pressure asymmetry amplitude with the main air flow rate is more substantial at the axial planes closer to the N3 vane leading edge plane. The above trends hold good for Expt. set II as well; the circumferential pressure asymmetry amplitude at all the axial locations in the outer shroud is lesser than Expt. set III and greater than Expt. set I.

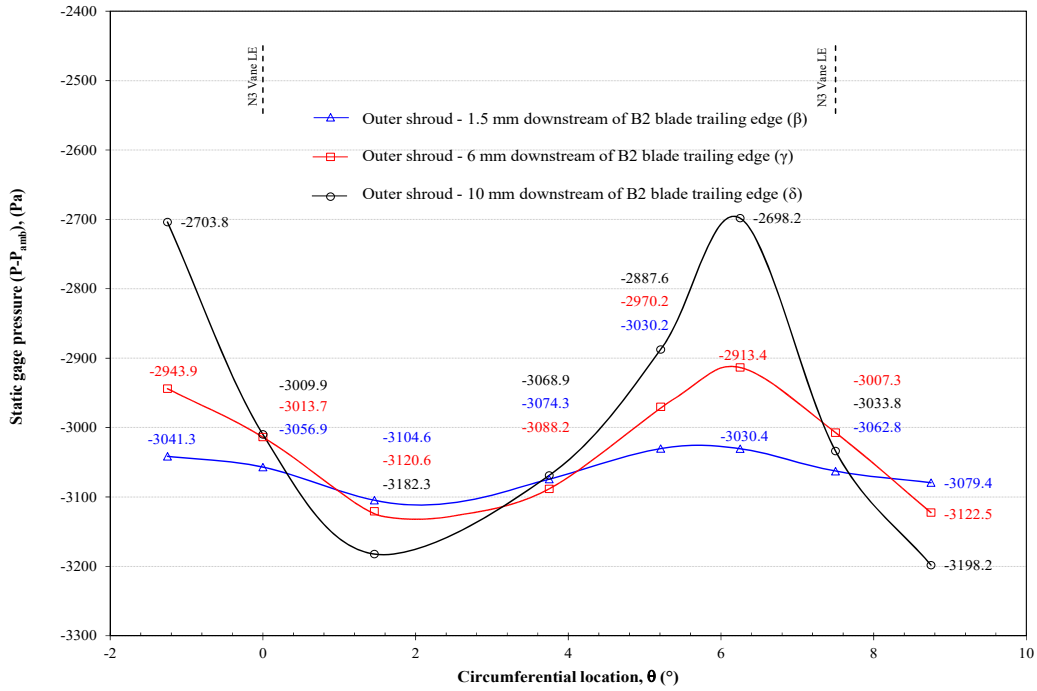

Fig. 3.13 Circumferential Distribution of Static Gage Pressure at Main Gas Annulus Outer Shroud (β, γ, δ planes) – Expt. Set I, $c_{w,a} = 2423$

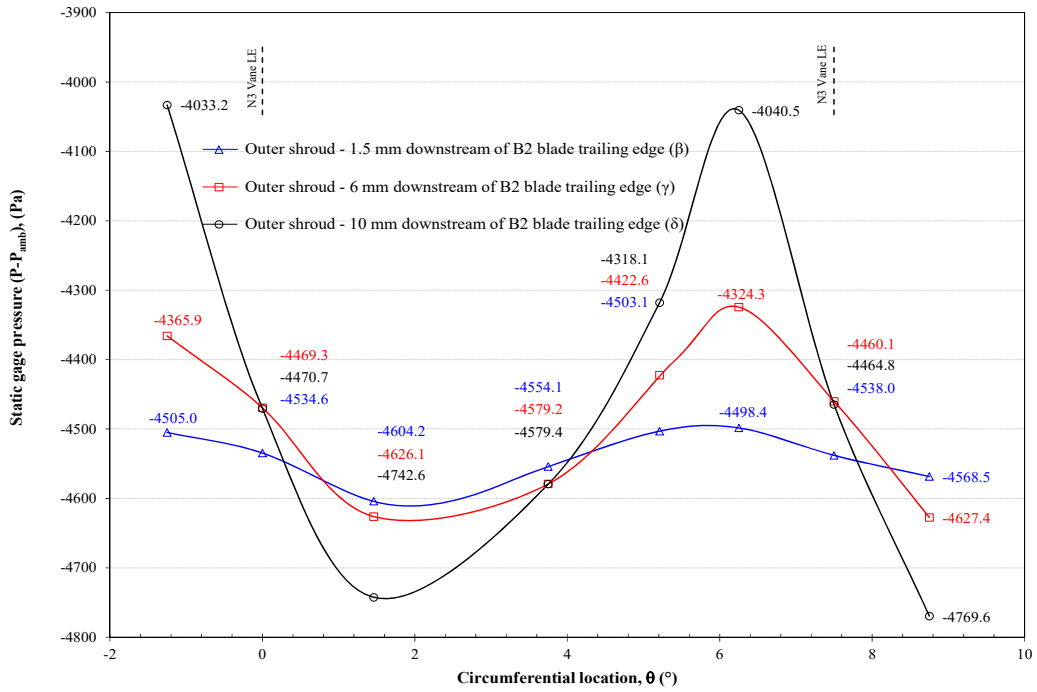

Fig. 3.14 Circumferential Distribution of Static Gage Pressure at Main Gas Annulus Outer Shroud (β, γ, δ planes) – Expt. Set III, $c_{w,a} = 2423$

Figures 3.15 and 3.16 show the circumferential distributions of time-averaged static gage pressure in the aft rim cavity stator surface at the radial locations r =200.4 mm (slightly radially inboard of N3 vane hub), r =195.2 mm and r =190.2 mm for Expt. Sets I and III at $c_{w,a}$ =2423 respectively. It is observed that for both the Expt. sets, the circumferential pressure asymmetry attenuates across the rim seal. While there is a slight pressure asymmetry at r = 195.2 mm and r = 190.2 mm for Expt. set III, there is no appreciable asymmetry for Expt. set I. The peak-to-trough pressure asymmetry amplitude at r = 200.4 mm increases with the main air flow rate. Comparing to the δ-plane in Figs. 3.13 and 3.14, for both the Expt. sets, the pressure level at r =200.4 mm is lower; the peak-to-trough pressure asymmetry amplitude at r =200.4 mm is significantly smaller than the δ-plane. The static pressure difference between representative locations in the main gas path and disk cavity is assumed to drive main gas ingestion. For the aft disk cavity, the difference in the static pressure measured at the radial location r = 200.4 mm (main gas path) and the rim cavity radial location r = 195.2 mm (disk cavity) is assumed to drive ingestion. Same trends were observed for Expt. set II as well.

Comparing Figs. 3.17, 3.18, 3.19 and 3.20 we observe that at the outer shroud axial locations and at the radial location r = 200.4 mm, the static pressure levels decrease with increase in purge air flow rate. The decrease in the static pressure level is more substantial at the radial location r = 200.4 mm. This trend holds good for Expt. set II as well. The trends at the radial locations r =195.2 mm and 190.2 mm are mixed for the three Expt. sets. It is to be noted that the static pressure level at r = 195.2 mm is higher than that of r = 190.2 mm for all three Expt. sets, at all purge air flow rates.

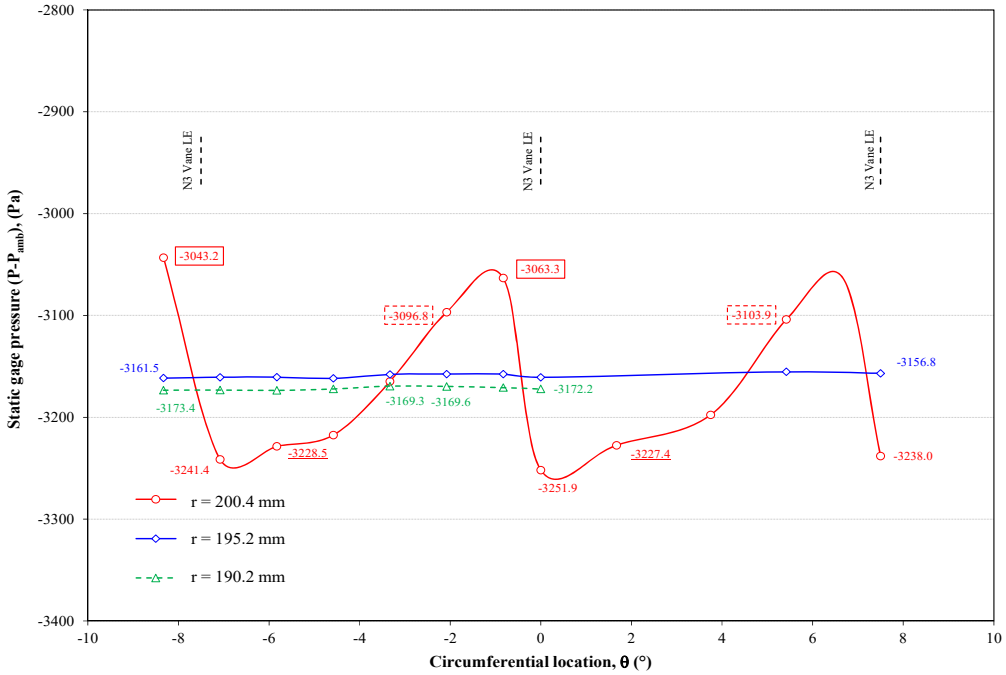

Fig. 3.15 Circumferential Distribution of Static Gage Pressure Near N3 Vane Hub at r = 200.4 mm and in the Aft Rim Cavity N3 Stator Surface at Two Radial Locations – Expt. Set I, $c_{w,a} = 2423$

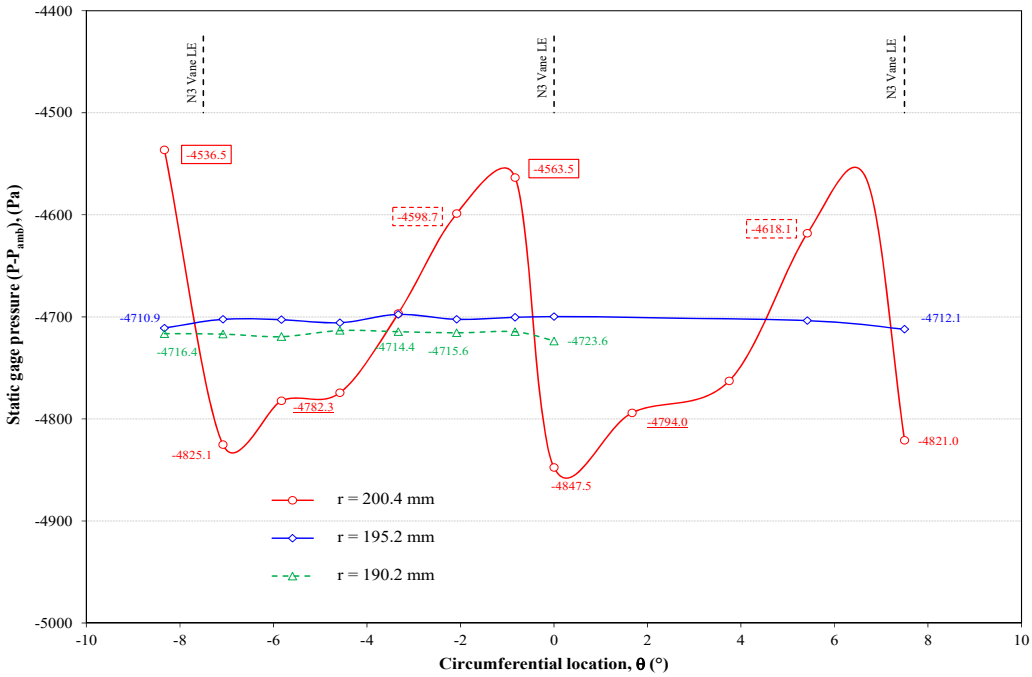

Fig. 3.16 Circumferential Distribution of Static Gage Pressure Near N3 Vane Hub at r = 200.4 mm and in the Aft Rim Cavity N3 Stator Surface at Two Radial Locations – Expt. Set III, $c_{w,a} = 2423$

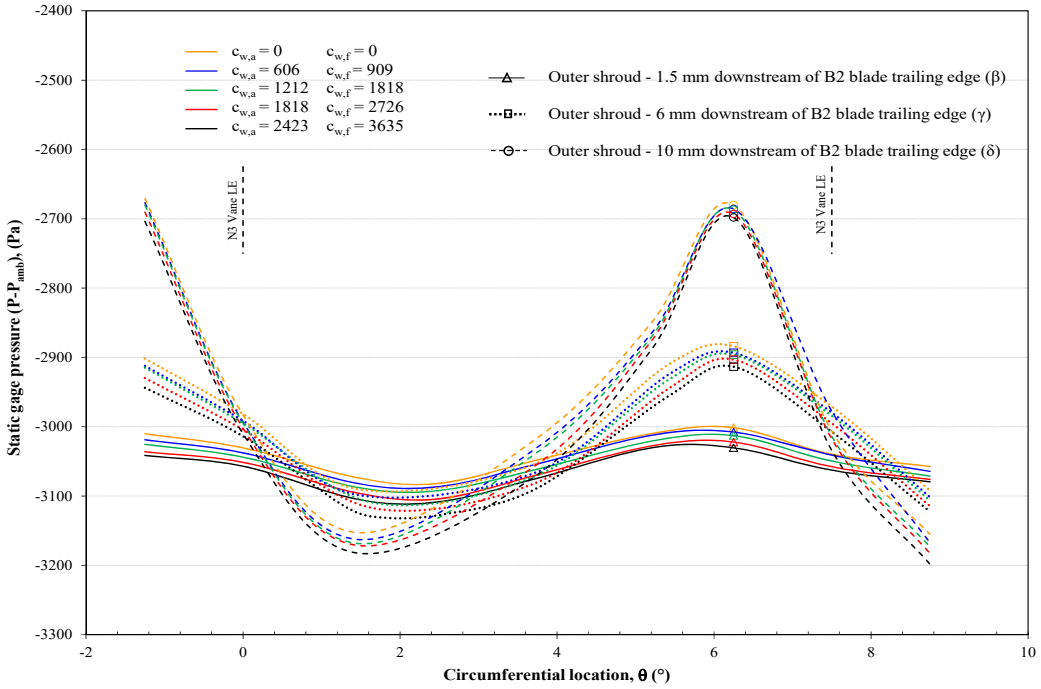

Fig. 3.17 Circumferential Distributions of Static Gage Pressure at Main Gas Annulus Outer Shroud (β, γ, δ planes) – Expt. Set I Conditions

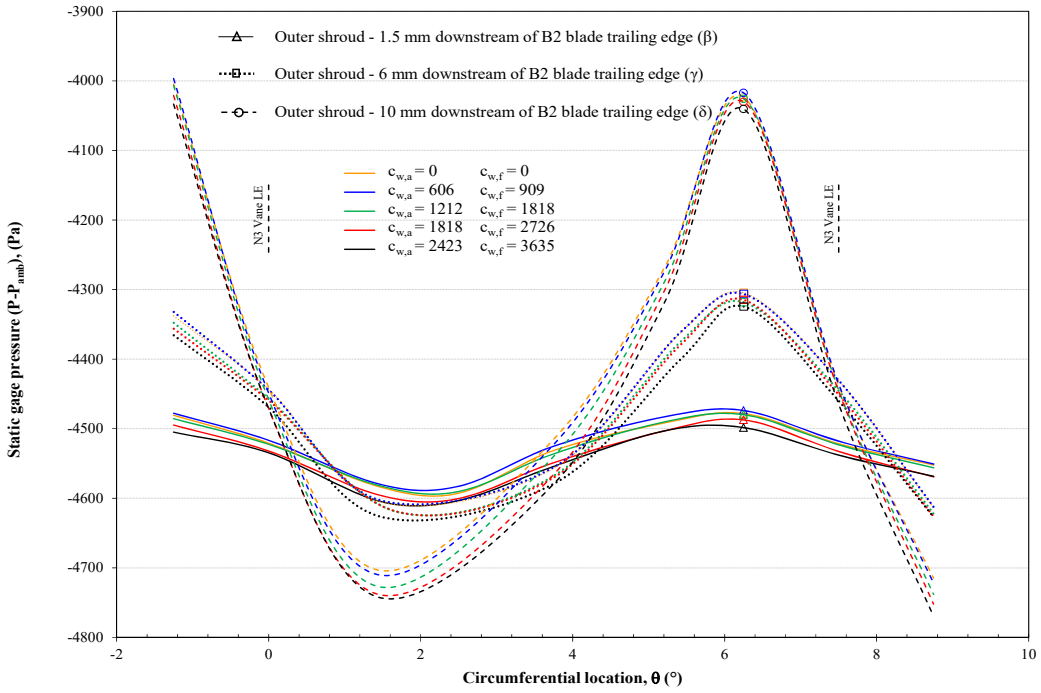

Fig. 3.18 Circumferential Distributions of Static Gage Pressure at Main Gas Annulus Outer Shroud (β, γ, δ planes) – Expt. Set III Conditions

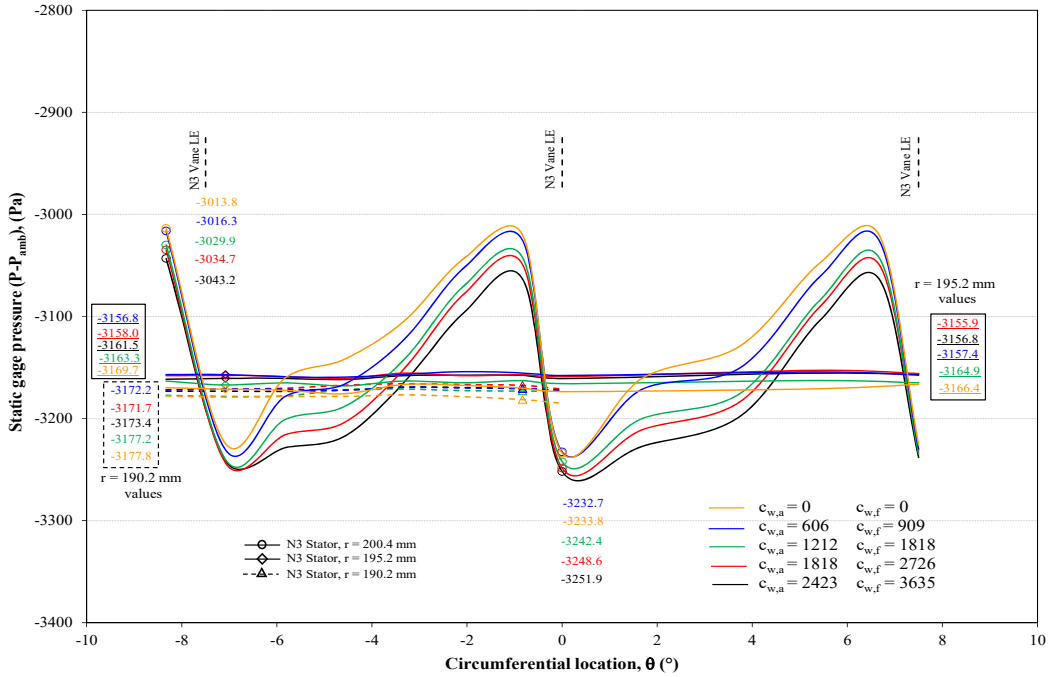

Fig. 3.19 Circumferential Distributions of Static Gage Pressure Near N3 Vane Hub at r = 200.4 mm and in the Aft Rim Cavity N3 Stator Surface at Two Radial Locations – Expt. Set I conditions.

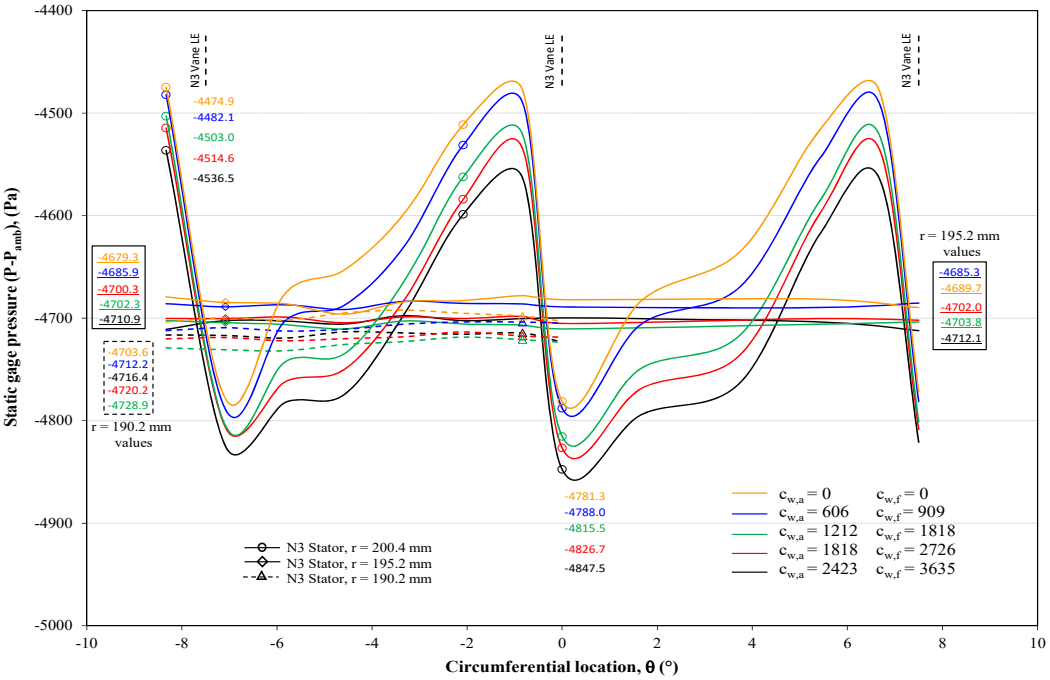

Fig. 3.20 Circumferential Distributions of Static Gage Pressure Near N3 Vane Hub at r = 200.4 mm and in the Aft Rim Cavity N3 Stator Surface at Two Radial Locations – Expt. Set III conditions.

Figures 3.21 and 3.22 show for Expt. sets I and III respectively, the radial distributions of time-averaged static gage pressure, in the aft disk cavity at N3 stator surface for the various purge air flow rates. From these figures it is observed that the static pressure level increases significantly with the purge air flow rate in the inner cavity. The pressure drop across the labyrinth seal increases with the purge air flow rate. This qualitatively points out that majority of the ingested air will progressively tend to be confined within the rim cavity, proving the labyrinth seal to be very effective in protecting the inner cavity.

In the rim cavity, the static pressure distributions for all the purge air flow rates were close to each other. This is because of the relatively unrestricted path of the purge air through the aft rim cavity in comparison to the front rim cavity. For clarity, the shape of the pressure distribution in the rim cavity is shown in insets for both the Expt. sets in their corresponding figures. The insets do not represent the actual trend of the static pressure distribution observed in the rim cavity while comparing various purge air flow rates, but maintain the shape of the pressure distribution for a particular purge air flow. Each distribution is offset along the ordinate by a constant value for clarity.

The radial pressure gradient observed in the rim cavity could be primarily due to the tangential motion (rotation) of the cavity fluid. The gradient decreases with increasing purge air flow rate. Similar trend is observed for Expt. set II as well.

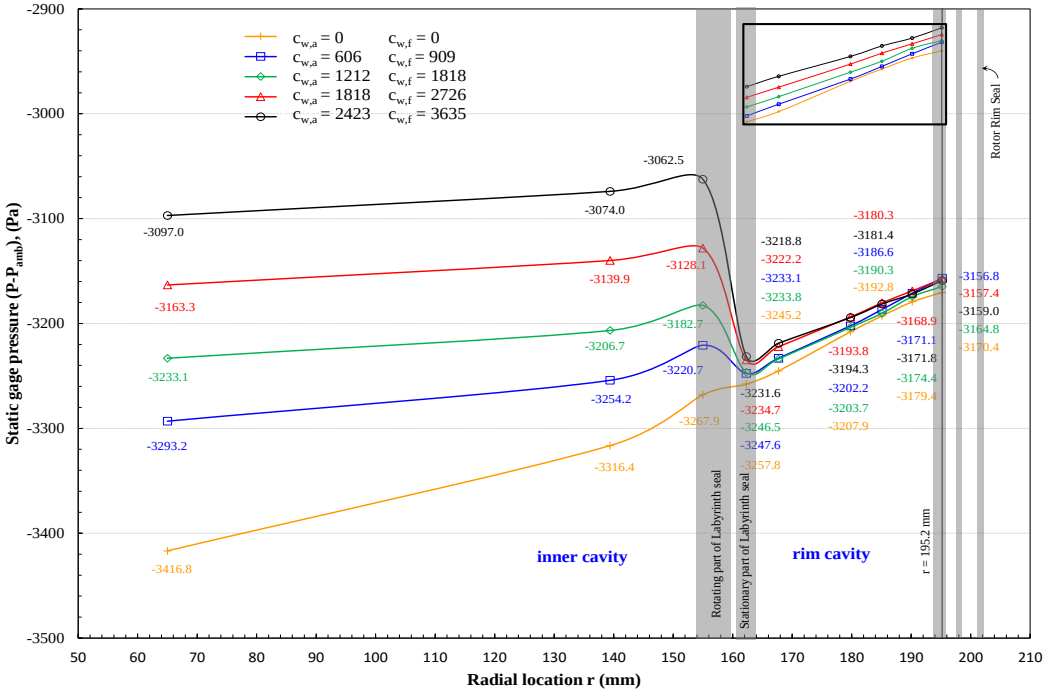

Fig. 3.21 Radial Distributions of Static Gage Pressure in the Aft Disk Cavity at N3 Stator Surface – Expt. Set I Conditions

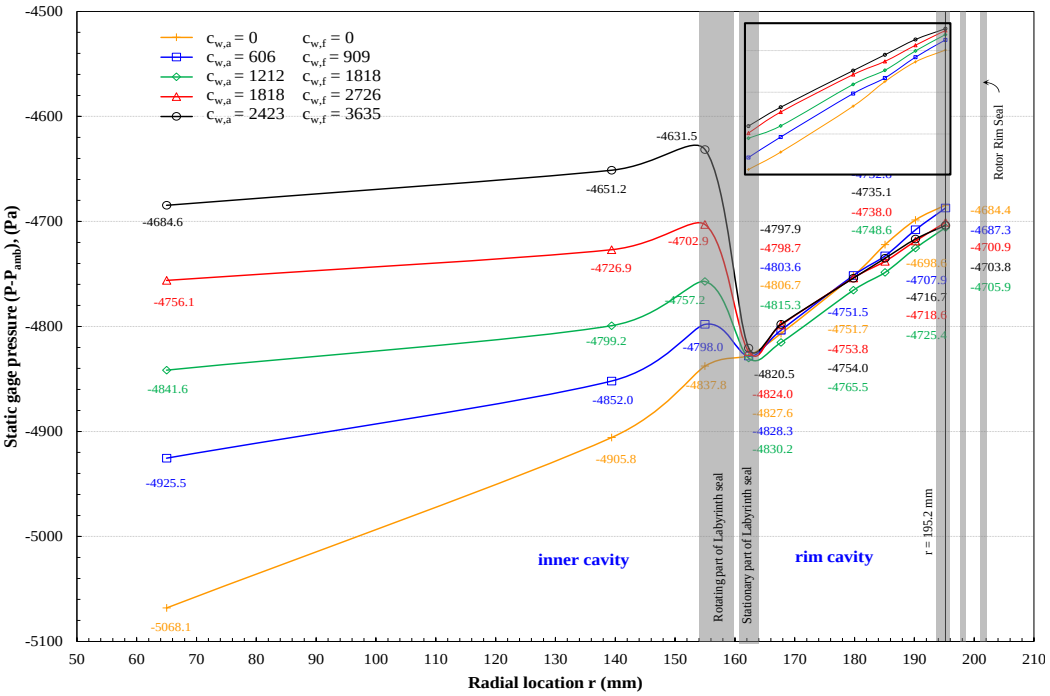

Fig. 3.22 Radial Distributions of Static Gage Pressure in the Aft Disk Cavity at N3 Stator Surface – Expt. Set III Conditions

3.3.2 Mainstream Gas Ingestion Distribution

Tracer gas (CO_2) concentration measurements were carried out at all the aft disk cavity locations (not in the outer shroud (β, γ and δ planes)) at which static pressure was measured. The sealing effectiveness is defined by Eq. 2.4.

CO_2 concentration was measured in the aft inner cavity at the radial locations r = 139.4 mm (four circumferential locations 90° apart) and r =65.0 mm (two circumferential locations 180°apart) for all three Expt. sets. It was observed that the mixing of CO_2 with the purge air in the supply pipe was complete prior to the inner cavity entry at the high purge air flow rates ($c_{w,f}$ = 2423, 1818) but becomes progressively incomplete at the two low purge air flow rates ($c_{w,f}$ = 1212, 606). It is reasoned that the 90° turn of the purge air flow after entering the inner cavity led to complete mixing at the low purge flows. As such, the circumferentially-averaged CO_2 concentration at the radial location r =139.4 mm is adopted as the CO_2 concentration in the purge air supplied (C_{purge}). This value was used in the calculation of sealing effectiveness for the entire aft disk cavity (rim as well as inner).

Figures 3.23 and 3.24 show for Expt. sets I and III the radial distributions of sealing effectiveness in the aft disk cavity at N3 stator surface. The sealing is perfect for all purge air flow rates in the inner cavity. There is a significant drop in effectiveness level across the labyrinth seal which decreases with the increase in purge air flow rate. In the rim cavity, there is substantial increase in sealing effectiveness with the purge air flow rate. The effectiveness levels for all the purge air flow rates of Expt. set I is higher than Expt. set III, due to the higher main air flow rate and rotor rotational speed for Expt. set III, favoring more ingestion. Similar trend was observed for Expt. set II; the effectiveness level at all four purge air flow rates was greater than Expt. set III and lesser than Expt. set I.

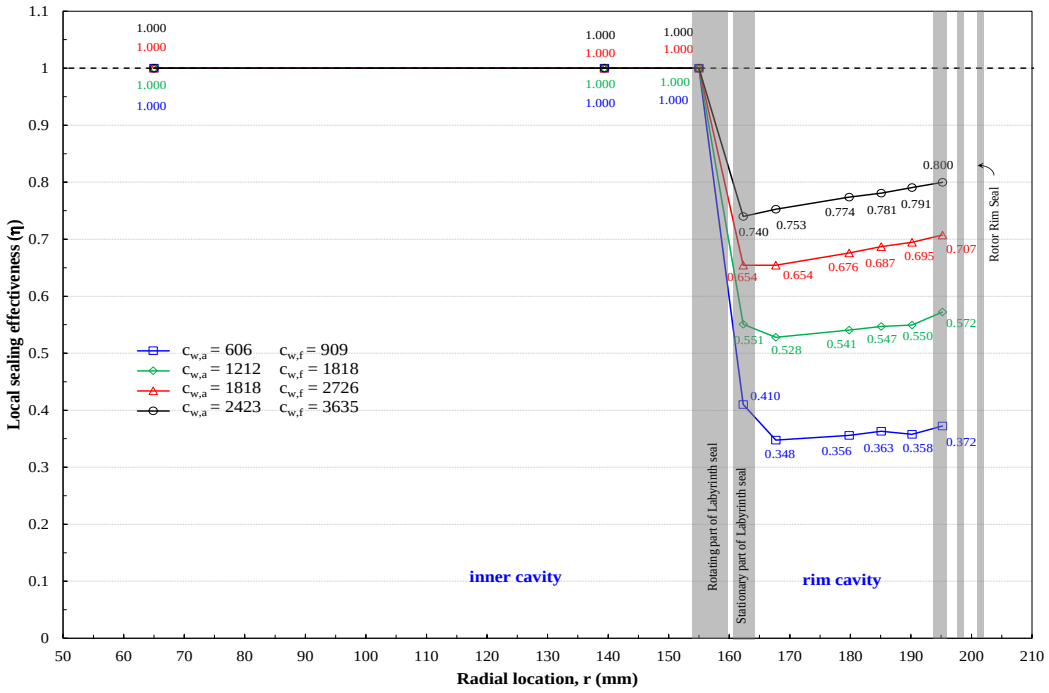

Fig. 3.23 Radial Distribution of Local Sealing Effectiveness in the Aft Rim Cavity at the N3 Stator Surface- Expt. Set I conditions

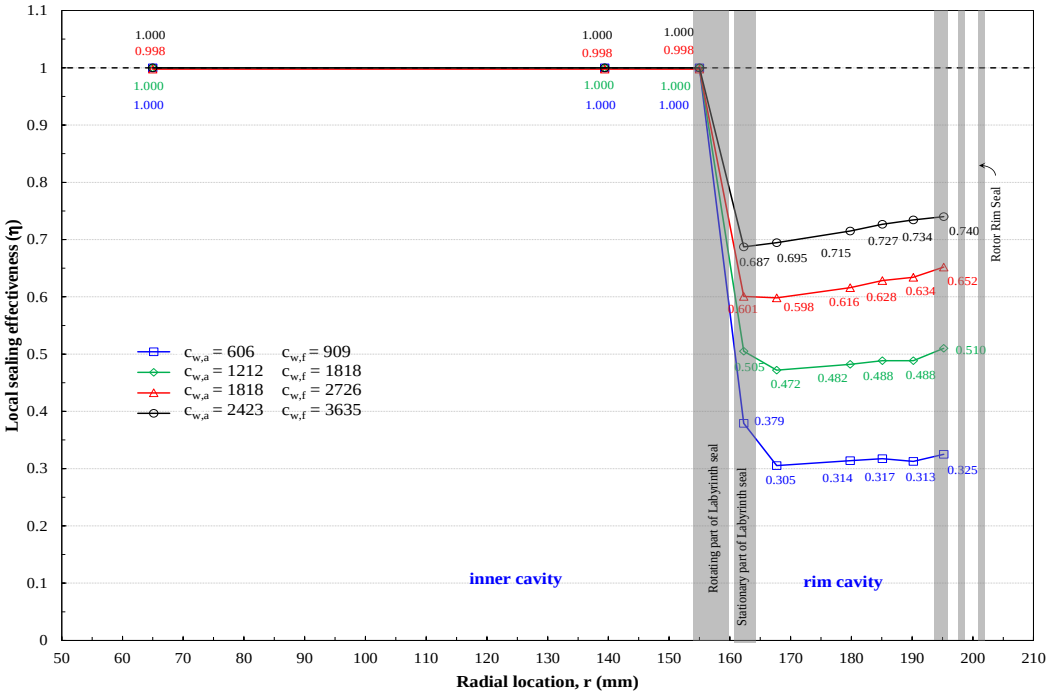

Fig. 3.24 Radial Distribution of Local Sealing Effectiveness in the Aft Rim Cavity at the N3 Stator Surface- Expt. Set III conditions

Compared to the front rim cavity, the sealing effectiveness level in the aft rim cavity is significantly lower. The reason is two-fold: (i) the purge air flow rates are lower (two-third of the front cavity), (ii) the double rim seal has no axial overlap.

Figure 3.25 shows the variation of sealing effectiveness with $c_{w,a}$ at the radial location r = 190.2 mm in the aft rim cavity at N3 stator surface for all three Expt. sets. Also, a best fit curve is drawn for each Expt. set. The sealing effectiveness increases gradually at all the purge air flow rates. The sealing effectiveness of Expt. sets I and II at this radial location is higher than that of Expt. set III for all purge air flows. A similar trend is observed at r = 195.2 mm.

Figure 3.26 shows the variation of sealing effectiveness with $c_{w,a}/Re_\phi$ (this is equal to $[V_{rim\ seal,a}/U].2\pi G_{c,a}$) for all three Expt. sets at the radial location r = 190.2 mm on the N3 stator surface. The data points fit onto a single curve. A similar trend is observed at the radial location r = 195.2 mm.

Figures 3.27 shows the variation of $c_{w,ing,a}$ with $c_{w,a}$ for all the three Expt. sets at the radial locations r =195.2 mm and r =190.2 mm on the N3 stator surface. Best-fit curves connect the corresponding data points. It is observed that the ingested flow decreases with increasing purge air flow rate. Expt. set III has more ingestion than Expt. sets I and II for all purge air flow rates due to the higher main air flow rate and rotor rotational speed.

Figure 3.28 shows the variation of $c_{w,ing,a}/c_{w,a}$ with $c_{w,a}/Re_\phi$ for all three Expt. sets at the radial locations r = 195.2 mm and r = 190.2 mm on the N3 stator surface. Best-fit curves are drawn to connect the corresponding data points of each radial location. The curves converge onto a single curve at higher values of $c_{w,a}/Re_\phi$. Also, the extrapolated

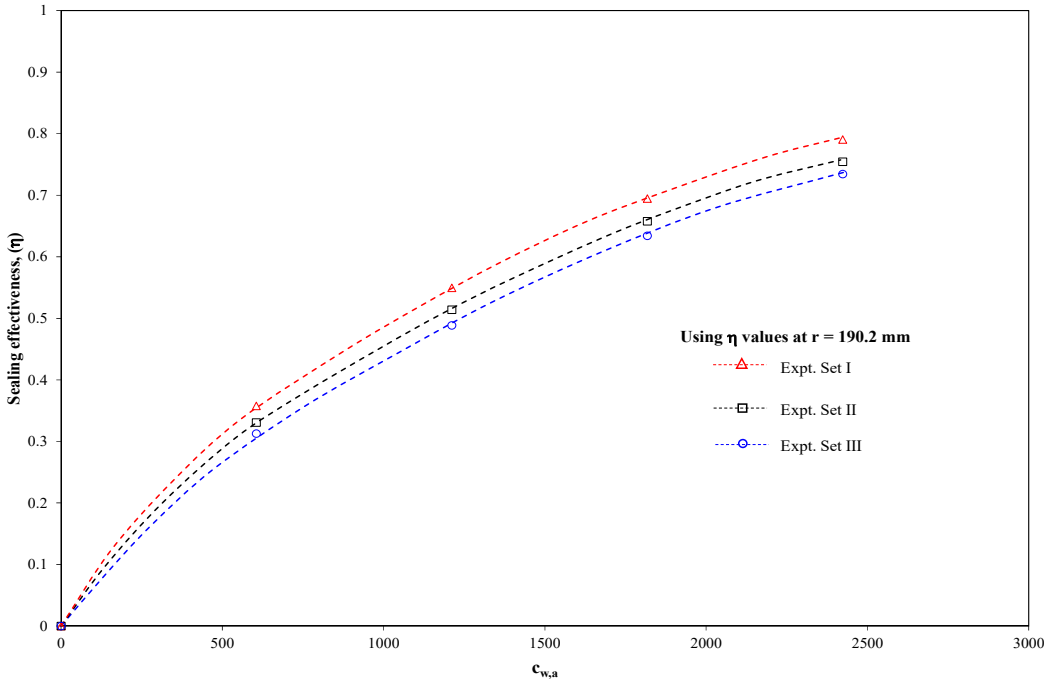

Fig. 3.25 Variation of Sealing Effectiveness with $c_{w,a}$ in the Aft Rim Cavity at N3 Stator Surface r = 190.2 mm for the Three Expt. Sets

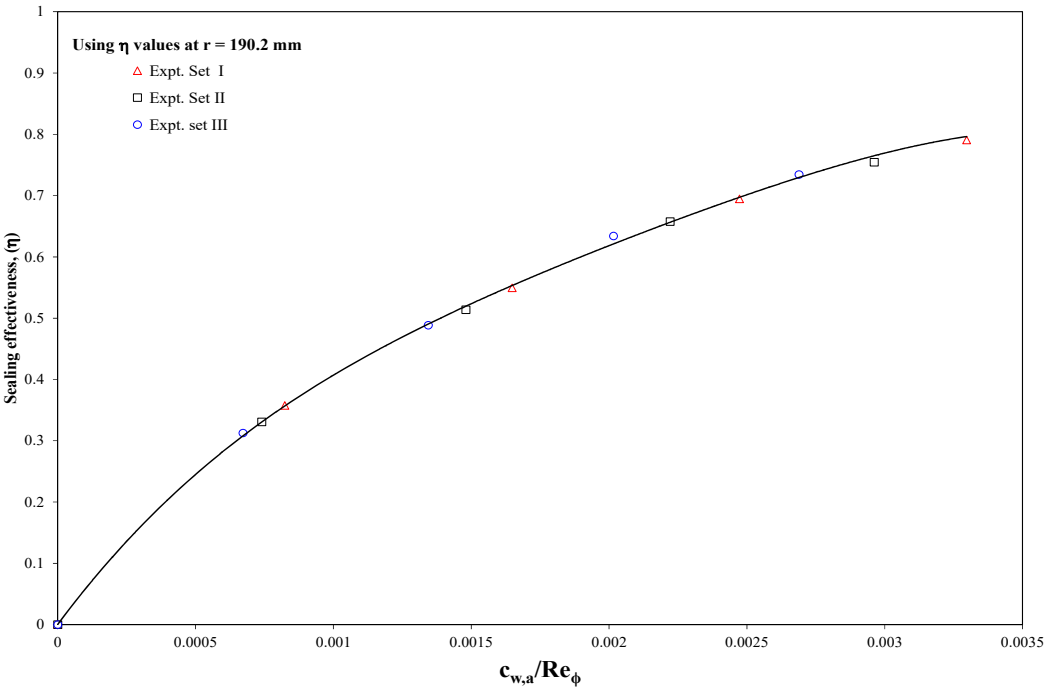

Fig. 3.26 Variation of Sealing Effectiveness with $c_{w,a}/Re_{\phi}$ in the Aft Rim Cavity at N3 Stator Surface r = 190.2 mm for the Three Expt. Sets

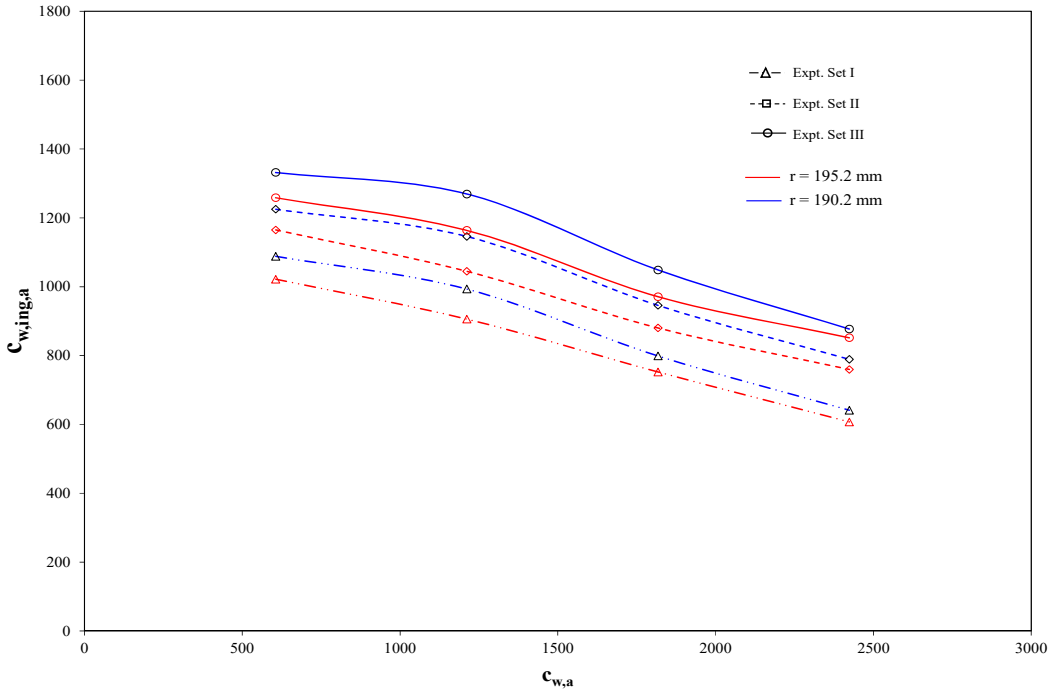

Fig. 3.27 Variation of $c_{w,ing,a}$ with $c_{w,a}$ in the Aft Rim Cavity at N3 Stator Surface r = 190.2 mm and 195.2 mm for the Three Expt. Sets

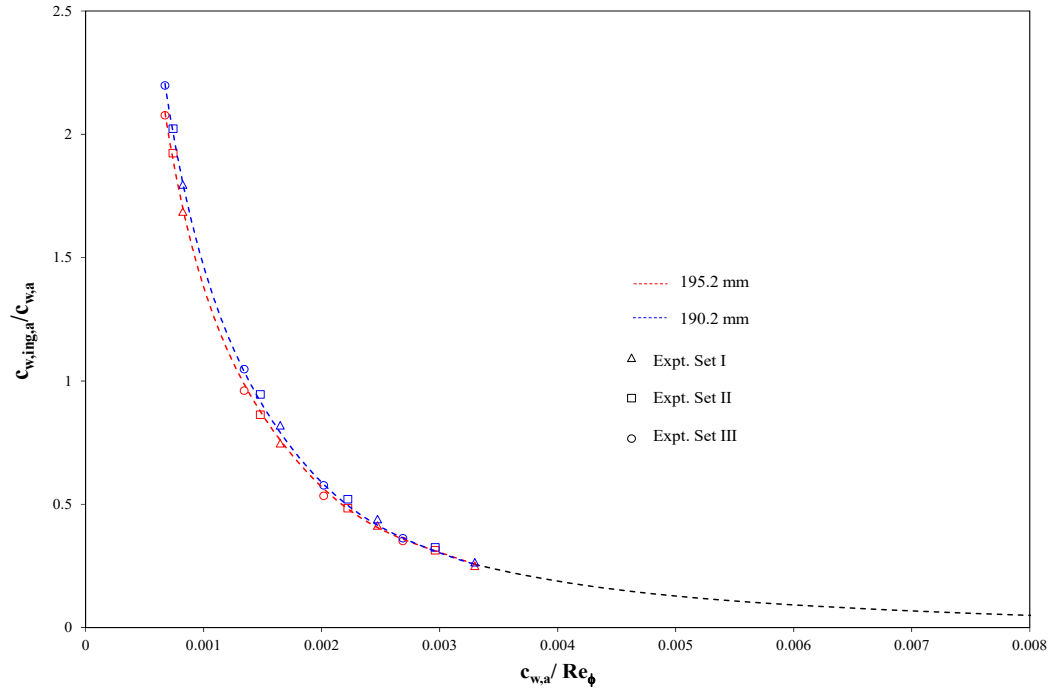

Fig. 3.28 Variation of $c_{w,ing,a}/c_{w,a}$ with $c_{w,a}/Re_{\phi}$ in the Aft Rim Cavity at N3 Stator Surface r = 190.2 mm and 195.2 mm for the Three Expt. Sets

curve tends to be asymptotic in nature which suggests that a performance limit exists for the aft rim seal as well, where increasing the purge air flow rate beyond a value would not help in reducing ingestion any further, and that the aft rim cavity would never be completely sealed.

The effectiveness values used for the above calculations at the two radial locations r =195.2 mm and r =190.2 mm were those obtained at their corresponding circumferential location aligned with a N3 vane leading edge.

CHAPTER 4

CONCLUDING REMARKS

Experiments were conducted in a subscale 1.5-stage axial flow air turbine featuring vanes and blades. The front cavity which is upstream of the rotor featured an axially overlapping radial clearance double seal at its rim while the aft cavity downstream of the rotor featured an axial clearance double rim seal. Both the cavities incorporate a labyrinth seal radially inboard which divided the disk cavity into an inner cavity (radially inboard) and a rim cavity (radially outboard).

Time-averaged static gage pressures were measured at various locations in the main gas path and in the disk cavities (front and aft cavities) to establish the steady-state pressure differentials that contribute to ingestion and egress. Tracer gas (CO_2) concentration was measured in each disk cavity through separate experiments, to quantify the ingestion of main gas into the cavity and evaluate the sealing effectiveness of the corresponding double rim seal. The experiment set with the highest main air flow rate and highest rotor rotational speed showed the most potential for main gas ingestion.

Main gas path

Time-averaged static pressure measurements in the main gas path showed that the peak-to-trough pressure asymmetry amplitude, which plays an important role in governing externally-induced ingestion, increases with the main air flow rate. The peak-to-trough pressure asymmetry increases as the N3 vane leading edge plane is approached.

Front disk cavity

The circumferential pressure asymmetry attenuated across the front disk cavity double rim seal for all three experiment sets at all purge air flow rates. Increasing the purge

air flow rate decreased the peak-to-trough pressure asymmetry amplitude at the vane platform and increased static pressure in the rim cavity, thereby reducing the potential for main gas ingestion into the cavity. Static pressure levels in the front inner cavity increased markedly with purge air flow rate increase. The radially inboard labyrinth seal proved to be very effective in sealing the inner cavity. The static pressure distribution near the rim seal showed that increasing the purge air flow rate progressively hindered the transportation of ingested past the seal at r = 194.4 mm, suggesting that much of the ingested air was confined to the wheelspace of the double rim seal and exhausted back into the main gas path.

Tracer gas concentration measurements showed that the front inner cavity sealing was near-perfect for all three experiment sets, at all purge air flows. The experiment set with the lowest main air flow rate and lowest rotor speed showed the highest sealing effectiveness level. It is suggested that EI ingestion dominated in the wheelspace radially outboard of the inner seal of the double rim seal, and rotationally induced ingestion dominated radially inboard of the inner seal of the double rim seal. Based on the concentration measurements, ingestion flow rate values ($c_{w,ing,f}$) for all three experiment sets were obtained at various radial locations in the front rim cavity . The largest ingestion mass flow rate occurred at r =198.0 mm on the front stator surface, suggesting that much of the ingested air flows back into the main annulus while a small fraction flows radially inboard of r =194.4 mm seal. Also, $c_{w,ing,f}$ values were higher for the experiment set with the highest main air flow rate and rotor speed. It was found that there existed a performance limit for the front double rim seal in that, the rim cavity was never completely sealed.

Aft disk cavity

The circumferential pressure asymmetry attenuated across the aft disk cavity double rim seal at all purge air flow rates for Expt. sets I and II; there remained a slight asymmetry radially outboard in the rim cavity at the highest main air flow rate (Expt. set III). There was significant increase in pressure level in the inner cavity as the purge air flow rate increased. The labyrinth seal proved to be very effective in sealing the inner cavity. The static pressure distributions in the rim cavity were close to each other at all purge air flows. The rim cavity static pressure distribution showed a positive radial gradient due to the tangential motion of the cavity fluid; this gradient decreased as the purge air flow rate increased.

Tracer gas concentration data showed that the inner cavity was completely sealed at all purge air flow rates for the three experiment sets. Sealing effectiveness increased significantly in the rim cavity as the purge air flow rate increased. The experiment set with the lowest main air flow rate and lowest rotor speed showed highest sealing effectiveness level. Ingestion mass flow rates ($c_{w,ing,a}$) were obtained from the concentration data for all three experiment sets at two rim cavity radial locations (r =195.2 mm and r =190.2 mm). The ingestion mass flow rate values were the highest for the experiment set with the highest main air flow rate and highest rotor speed. It was found that there existed a performance limit for the aft double rim seal in that, the rim cavity was never completely sealed.

REFERENCES

[1] "Airplane Flying Handbook", U.S. Department of Transportation, Federal Aviation Administration, FAA-H-8083-3A.

[2] “The Jet Engine”, 5th Edition, Rolls-Royce plc 1986, ISBN0 902121 2 35.

[3] Batchelor, G. K. (1951). Note on a class of solutions of the Navier-Stokes equations representing steady rotationally-symmetric flow. The Quarterly Journal of Mechanics and Applied Mathematics, 4(1), 29-41.

[4] Daily, J. W., & Nece, R. E. (1960). Chamber dimension effects on induced flow and frictional resistance of enclosed rotating disks. ASME Journal of Fluids Engineering, 82(1), pp. 217-230.

[5] Bayley, F. J., & Owen, J. M. (1970). The fluid dynamics of a shrouded disk system with a radial outflow of coolant. ASME Journal of Engineering for Gas Turbines and Power, 92(3), pp. 335-341.

[6] Phadke, U. P., & Owen, J. M. (1983). An investigation of ingress for an “air-cooled” shrouded rotating disk system with radial-clearance seals. ASME Journal of Engineering for Gas Turbines and Power, 105(1), pp.178-182.

[7] Dring, R. P., Joslyn, H. D., Hardin, L. W., & Wagner, J. H. (1982). Turbine rotor-stator interaction. Journal of Engineering for Gas Turbines and Power, 104(4), pp. 729-742.

[8] Phadke, U. P., & Owen, J. M. (1988). Aerodynamic aspects of the sealing of gas-turbine rotor-stator systems: Part 1: The behavior of simple shrouded rotating-disk systems in a quiescent environment. International journal of heat and fluid flow, 9(2), pp. 98-105.

[9] Phadke, U. P., & Owen, J. M. (1988). Aerodynamic aspects of the sealing of gas-turbine rotor-stator systems: Part 2: The performance of simple seals in a quasi-axisymmetric external flow. International journal of heat and fluid flow, 9(2), pp. 106-112.

[10] Phadke, U. P., & Owen, J. M. (1988). Aerodynamic Aspects of the Sealing of Gas-Turbine Rotor-Stator Systems: Part 3: The Effect of Nonaxisymmetric External Flow on Seal Performance. International journal of heat and fluid flow, 9(2), pp. 113-117.

[11] Abe, T., Kikuchi, J., & Takeuchi, H. (1979). ‘An Investigation of Turbine Disk Cooling (Experimental investigation and observation of hot gas flow into a wheel space) Paper GT30, 13th International Conference on Combustion Engines, Vienna.

[12] Dadkhah, S., Turner, A. B., & Chew, J. W. (1992). Performance of radial clearance rim seals in upstream and downstream rotor–stator wheelspaces, ASME Journal of Turbomachinery, 114(2), pp. 439-445.

[13] Johnson, B. V., Mack, G. J., Paolillo, R. E., & Daniels, W. A. (1994). Turbine rim seal gas path flow ingestion mechanisms. AIAA paper, (94-2703).

[14] Bohn, D., Johann, E., & Krüger, U. (1995). Experimental and numerical investigations of aerodynamic aspects of hot gas ingestion in rotor-stator systems with superimposed cooling mass flow. In ASME 1995 International Gas Turbine and Aeroengine Congress and Exposition (pp. V001T01A034-V001T01A034). American Society of Mechanical Engineers.

[15] Green, T., & Turner, A. B. (1994). Ingestion into the upstream wheelspace of an axial turbine stage. Journal of turbomachinery, 116(2), 327-332.

[16] Roy, R. P., Xu, G., Feng, J., & Kang, S. (2001). Pressure field and main-stream gas ingestion in a rotor-stator disk cavity. In ASME Turbo Expo 2001: Power for Land, Sea, and Air (pp. V003T01A089-V003T01A089). American Society of Mechanical Engineers.

[17] Roy, R. P., Devasenathipathy, S., Xu, G., & Zhao, Y. (1999). 'A Study of the Flow Field in a Model Rotor–Stator Disk Cavity. ASME Paper, 99-GT-246.

[18] Roy, R. P., Xu, G., & Feng, J. (2000). Study of main-stream gas ingestion in a rotor-stator disk cavity. AIAA Paper No 2000-3372.

[19] Roy, R.P., Zhou, D.W., Ganesan, S., Wang, C.-Z., Paolillo, R.E., and Johnson, B.V., 2007, "The Flow Field and Main Gas Ingestion in a Rotor-Stator Disk Cavity", ASME Paper GT2007-27671

[20] Zhou, D.W., Roy, R.P., Wang, C.-Z., and Glahn, G.A., 2011, "Main Gas Ingestion in a Turbine Stage for Three Rim Cavity Configurations", ASME Journal of Turbomachinery, Vol. 133, pp. 031023-1 - 031023-12.

[21] Balasubramanian, J., Junnarkar, N., Roy, R. P., & Glahn, J. A. (2012). Disk cavity purge air outflow into the main gas path of a model turbine stage. Experimental Thermal and Fluid Science, 38, 266-269.

[22] Balasubramanian, J., Pathak, P. S., Thiagarajan, J.K., Singh, P., Roy, R.P., and Mirzamoghadam, A. V., 2015, "Experimental study of Ingestion in the Rotor-Stator Disk Cavity of a Subscale Axial Turbine Stage", ASME. J. Turbomachinery, 137(9), pp. 091010-1 – 091010-10.

[23] Narzary, D., Feng, J., Roy, R. P., & Paolillo, R. E. (2005). Ingestion Into a Rotor-Stator Disk Cavity With Single and Double Rim Seals. In 41st AIAA Joint Propulsion Conference, Tucson, Arizona, Paper No. AIAA-2005-3982.

[24] Bohn, D. E., Decker, A., Ma, H., and Wolff, M., 2003, "Influence of Sealing Air Mass Flow on the Velocity Distribution In and Inside the Rim Seal of the Upstream Cavity of a 1.5 Stage Turbine," ASME Paper No. GT2003-38459.

[25] Jakoby, R., Zierer, T., Lindblad, K., Larsson, J., deVito, L., Bohn, D. E., Funcke, J., and Decker, A., 2004, "Numerical Simulation of the Unsteady Flow Field in an Axial Gas Turbine Rim Seal Configuration," ASME Paper No. GT2004-53829.

[26] Bohn,D.E., Decker, A., and Ohlendorf, N., 2006, "Influence of Radial and Axial Rim Seal Geometry on Hot Gas Ingestion into the Upstream Cavity of a 1.5 Stage Turbine," ASME Paper No. GT2006-90453.

[27] Johnson, B.V., Wang, C.-Z., and Roy, R.P., 2008, "A Rim Seal Orifice Model with Two Cd's and Effects of Swirl in Seals", ASME Paper No. GT2008 – 50650.

[28] Balasubramanian, J., Junnarkar, N., Zhou, D. W., Roy, R. P., Kim, Y. W., and Moon, H. K., 2011, "Experiments on Aft-Disk Cavity Ingestion in a Model 1.5-Stage Axial-Flow Turbine," ASME Paper No. GT2011–45895.

[29] Rabs, M., Benra, A. F., Dohmen, J. H., and Schneider, O., 2009, "Investigation of Flow Instabilities near the Rim Cavity of a 1.5 Stage Gas Turbine," ASME Paper No. GT2009-59965.

[30] Luo, X., Liu, D., Wu, H., and Tao, Z., 2014 "Particle Image Velocimetry Measurement and Computational Fluid Dynamic Simulations of the Unsteady Flow Within a Rotating Disk Cavity," ASME J. Eng. Gas Turbines Power, 136(11), pp.112601-1 – 112601-6.

[31] Teuber, R., Li, Y.S., Maltson, J., Wilson, M., Lock, G.D., Owen, J. M., 2012, "Computational Extrapolation of Turbine Sealing Effectiveness from Test Rig to Engine Conditions", ASME IGTI paper GT2012-68490.

[32] Owen, J. M., Zhou, K., Pountney, O., Wilson, M., & Lock, G. (2012). Prediction of Ingress Through Turbine Rim Seals—Part I: Externally Induced Ingress. Journal of Turbomachinery, 134(3),pp. 031012-1 - 031012-13.

[33] Sangan, C. M., Pountney, O. J., Zhou, K., Wilson, M., Owen, J. M., & Lock, G. D. (2013). Experimental Measurements of Ingestion Through Turbine Rim Seals—Part I: Externally Induced Ingress, ASME Journal of Turbomachinery, 135(2), pp. 021012-1-021012-10.

[34] Sangan, C. M., Pountney, O. J., Zhou, K., Owen, J. M., Wilson, M., & Lock, G. D. (2013). Experimental Measurements of Ingestion Through Turbine Rim Seals—Part II: Rotationally Induced Ingress, ASME Journal of Turbomachinery, 135(2),pp. 021013-1–021013-9.

[35] Sangan, C. M., Pountney, O. J., Scobie, J. A., Wilson, M., Owen, J. M., & Lock, G. D. (2013). Experimental Measurements of Ingestion Through Turbine Rim Seals—Part III: Single and Double Seals, ASME Journal of Turbomachinery, 135(5), pp. 051011-1-051011-11.

[36] Owen, J. M. (2012). Theoretical modelling of hot gas ingestion through turbine rim seals. Propulsion and Power Research, 1(1),pp. 1-11.

[37] Bhavnani, S.H., Khilnani, V.I., Tsai, L.-C., Khodadadi, J.M., and Goodling, J.S., 1992, "Effective Sealing of a Disk Cavity Using a Double-Toothed Rim Seal", ASME Paper 92-GT-379.

[38] Scobie JA, Teuber R, Sheng Li Y, Sangan CM, Wilson M, Lock GD. Design of an Improved Turbine Rim-Seal. ASME. J. Eng. Gas Turbines Power. 2015;138(2):022503-022503-10. doi:10.1115/1.4031241.

[39] Sangan CM, Scobie JA, Michael Owen JJ, Lock GD, Tham K, Laurello VP. Performance of a Finned Turbine Rim Seal. ASME. J. Turbomach. 2014;136(11):111008-111008-10. doi:10.1115/1.4028116.

[40] Roy, R.P., Feng, J., Narzary, D., and Paololllo, R.E., 2005, “Experiment on Gas Ingestion Through Axial-Flow Turbine Rim Seals”, ASME Journal of Engineering for Gas Turbines and Power, Vol. 127. 127, pp.573-582.

[41] Owen, J. M., and Rogers, R. H., 1989, Flow and Heat Transfer in Rotating-Disc Systems, Volume 1—Rotor Stator Systems, Research Studies Press Ltd.,Taunton, UK.

[42] Ganesan, S. (2007). Flow Field in a Rotor-stator Disk Cavity with and Without Preswirled Secondary Air, M.S. Thesis, Arizona State University.

[43] Balasubramanian, J. H. (2010). Experimental Study of Main Gas Ingestion and Purge Gas Egress Flow in Model Gas Turbine Stages, M.S. Thesis, Arizona State University.

[44] Pathak, P. (2013). Experimental Study of the Flow Field in a Model Rotor-Stator Disk Cavity Using Particle Image Velocimetry, M.S. Thesis, Arizona State University.

[45] Thiagarajan, J. K. (2013). Experimental Study of Pressure and Main Gas Ingestion Distributions in a Model Rotor-Stator Disk Cavity, M.S. Thesis, Arizona State University.

[46] Singh, P. (2014). Characterization of Ingestion through the Rim Seal of Rotor-Stator Disk Cavity in a Subscale Single-Stage Axial Turbine, M.S. Thesis, Arizona State University.